ACCEPTED VERSION

Dahe Gu, Zhiwei Sun, Bassam B. Dally, Paul R. Medwell, Zeyad T. Alwahabi, Graham J. Nathan

Final publication at http://dx.doi.org/10.1016/j.combustflame.2017.01.017

PERMISSIONS

https://www.elsevier.com/about/our-business/policies/sharing

Accepted Manuscript

Authors can share their accepted manuscript:

[24 months embargo]

After the embargo period

- via non-commercial hosting platforms such as their institutional repository
- via commercial sites with which Elsevier has an agreement

In all cases accepted manuscripts should:

- link to the formal publication via its DOI
- bear a CC-BY-NC-ND license – this is easy to do
- if aggregated with other manuscripts, for example in a repository or other site, be shared in alignment with our hosting policy
- not be added to or enhanced in any way to appear more like, or to substitute for, the published journal article

12 April 2022

---

http://hdl.handle.net/2440/105863

Simultaneous measurements of gas temperature, soot volume fraction and primary particle diameter in a sooting lifted turbulent ethylene/air non-premixed flame

Dahe Gu[1,2, *], Zhiwei Sun[1,2], Bassam B. Dally[1,2], Paul R. Medwell[1,2], Zeyad T. Alwahabi[1,3], Graham J. Nathan[1,2]

[1]*Centre for Energy Technology, The University of Adelaide, S.A. 5005, Australia*
[2]*School of Mechanical Engineering, The University of Adelaide, S.A. 5005, Australia*
[3]*School of Chemical Engineering, The University of Adelaide, S.A. 5005, Australia*

Dahe Gu
Email address: dahe.gu@adelaide.edu.au
Graham Nathan
Email address: graham.nathan@adelaide.edu.au

Abstract

Simultaneous, planar measurements of flame temperature (T), soot volume fraction (f_v), primary particle diameter (d_p) and the derived number density of primary particles (N_p) are reported in a well characterized, lifted ethylene jet diffusion flame, both to increase confidence in measurement accuracy and to provide new joint statistics. Planar measurements of temperature were performed using non-linear excitation regime two-line atomic fluorescence (nTLAF) of indium with an improved optical arrangement over those reported previously, and were found to yield good agreement with previous measurements obtained with coherent anti-Stokes Raman spectroscopy (CARS). Planar measurements of soot volume fraction and primary particle diameter were performed using time-resolved laser-induced incandescence (TiRe-LII). On the flame centreline, both the measured values of d_p and f_v grow with axial distance to peak near to the mid height of the flame. The joint probability density functions (PDF) of the measured T, f_v, d_p and derived N_p were obtained from the two-dimensional images and assessed at 15 locations in the flame (5 radial × 3 axial locations). Strong correlations were found between f_v, d_p and N_p, while they exhibit a moderate correlation with flame temperature. The changes in PDFs with radial and axial locations and the most probable values are also reported.

Keywords: *flame temperature, soot volume fraction, primary particle diameter, turbulent flame, simultaneous and planar measurement*

1. Introduction

Reliable measurements of well characterised turbulent sooting flames are needed to support the development and validation of predictive models, which in turn are needed to mitigate soot emissions from practical combustion systems that cause deleterious effects on human health and climate change [1-3]. It is also highly desirable that such measurements not only be well resolved spatially and temporally, but also record multiple parameters simultaneously and in multiple dimensions, due to the complex coupling between soot, turbulence, radiation and chemistry. Of these, four parameters of particular interest for modelling soot evolution are soot volume fraction (f_v), primary particle diameter (d_p), number density of primary soot particle (N_p) and flame temperature (T), which influence radiative heat transfer in turbulent flames. However, measurements of these key parameters are rare. Previous studies reported measurements of planar f_v and laser-induced fluorescence (LIF) of polycyclic aromatic hydrocarbons (PAHs) [4], of simultaneous f_v and qualitative hydroxyl radical (OH) concentrations [5] and of simultaneous f_v and velocity [6]. Only a few simultaneous measurements have been reported of T and f_v in turbulent jet flames [7-10] and in pool fires [11, 12] and of f_v, d_p and N_p in turbulent flames [13-15]. However, none of these are well resolved both spatially and temporally and of known absolute accuracy, which is desirable for model validation. There is therefore a need for new, more accurate and comprehensive data in a well-characterized flame.

A vital aspect of determining absolute measurement accuracy is the need for independent measurements of identical and well characterized flames with different methods. However, to date, such independent assessments in turbulent sooting flames are rare, due the challenges of performing measurement of key parameters in these environments [16]. For this reason, such measurements are yet to be performed for T, f_v, d_p and N_p. While data are available for several target turbulent sooting flames [17-21], the measurements reported by Köhler *et al.* [17, 21] are particularly relevant. This is a non-premixed lifted turbulent ethylene/air jet flame with a relatively simple burner configuration, a well-studied fuel of ethylene and sufficient soot concentration for accurate measurement. These characteristics satisfy modelers' needs regarding boundary conditions and flame characteristics [22, 23]. Moreover, the authors performed comprehensive optical measurements, including flame temperature using shifted-vibrational coherent anti-Stokes Raman spectroscopy (CARS), flow velocity using particle image velocimetry, f_v using planar laser-induced incandescense (PLII) and planar laser-induced fluorescence (PLIF) of OH and PAHs [17, 21]. This relatively extensive data set makes this flame a good candidate firstly for assessment of measurement accuracy through independent measurements, for example, of T and f_v, secondly, for the provision of new insight and data, though the simultaneous (and planar) measurements.

A key statistical parameter that is desired for the above flame is the joint probability density function (PDF) of T and f_v, which is important for accurate predictions of radiation and validation of soot models. Very limited data of the joint PDFs of these two key parameters are available [7-12], which is attributed to the challenging environments encountered by the diagnostic techniques for simultaneous planar measurements. In particular, simultaneous measurements of f_v using laser-beam extinction and soot particle temperature using two-color pyrometry were performed in piloted ethylene jet flames [7-10] and in JP-8 pool fires [11, 12]. This, involves a semi-intrusive, two-ended optical-fiber probe, which integrates over a length of 5 or 10 mm. Alternative non-intrusive optical thermometry methods, such as CARS, are challenging to perform concurrently with the LII technique and have only moderate spatial resolution, typically of a few of millimeters [17, 21]. Simultaneous and instantaneous imaging of T and f_v with a high spatial resolution of ~ 400 μm, using nTLAF and PLII, has been demonstrated [18, 24]. However, these flames do not have sufficient soot concentration with peak f_v below 1.0 ppm and the temperature measurements by Mahmoud *et al.* [18] have a relatively high uncertainty (~ 180 K). Significantly, this work does not

provide joint PDFs of T and f_v [18, 24]. Hence, there is a need for reliable joint PDFs in turbulent sooting flames, such as the chosen target flame studied by Köhler *et al.* [17, 21]. The present study is driven not only by the need for complete data in well characterized flames, but also by the need for comparison of such data with previous measurements of the joint PDFs in other flames. There is also a need for a quantitative comparison of the accuracy of the nTLAF method against the more well-established CARS method. Such a direct comparison is yet to be reported in turbulent sooting flames and is sought after prior to the application of nTLAF in highly turbulent sooting flames to provide dataset for model validation.

The measurements of N_p and d_p are also important to advance understanding of the mechanisms of soot formation and oxidation and validation of soot models. However, available experimental data on N_p and/or d_p are mostly limited to laminar flames [25, 26] and are rare for turbulent flames [14], especially that of simultaneous and planar data. While the thermophoretic sampling technique can provide reliable and statistical information [27, 28], it has been limited to point-wise measurements. The utilization of Rayleigh scattering and LII imaging for measurements of N_p and d_p suffers from the assumption of scattering behavior for soot aggregates is neglected [29] and has unknown accuracy in non-premixed turbulent flames. Planar measurements of d_p in atmospheric flames with time-resolved laser-induced incandescence (TiRe-LII) has been found to yield good agreement with results obtained with sampling thermophoretic method [30]. However, TiRe-LII has mostly been applied to steady laminar flames [25, 26], with one exception of using four sequential LII images in an unsteady premixed flame [31]. Therefore, there is a need to extend the application of the instantaneous planar TiRe-LII technique into the turbulent flames, both to advance the ongoing development of the TiRe-LII technique and to provide measurements of d_p in turbulent flames, as well as values of N_p, which can be derived from the measured values of d_p and f_v.

In light of the background described above, the present work firstly assessed the accuracy of nTLAF through comparison with previous results measured with CARS in the selected turbulent sooting flame. Then, simultaneous and planar measurements of T, f_v and d_p using the combination of nTLAF with TiRe-LII were performed at 15 different heights in the flame. The measurements of f_v and d_p along the flame centerline were also compared with previous experimental and simulation results. The radial profiles and the joint PDFs of the four key parameters, i.e. T, f_v, d_p and N_p, are also presented.

2. Experimental arrangement

2.1 Burner configuration

The lifted non-premixed turbulent ethylene flame of Köhler *et al.* [17, 21] was chosen to allow for direct comparison of their measurements of T and f_v to the data acquired in the present study. The burner consists of a stainless steel tube with an inner diameter (d) of 2.0 mm and an outer diameter of 6.0 mm. The fuel tube is tapered from the outer edge to a sharp edge at the exit nozzle over a distance of 10 mm. A co-flow of air flow was delivered through a contraction with a square cross-section of 310 mm × 310 mm at the upstream end, converging to 150 mm × 150 mm over a distance of 450 mm, which differs slightly from the previous geometry [17, 21]. The tip of fuel tube extends 50 mm above the air co-flow nozzle. The burner was mounted vertically and positioned ~ 1.5 m beneath an exhaust hood and no influence of the exhaust hood on the flame was observed. The burner was mounted on a traverse to translate the burner, with the hood, through the optical measurement system.

The flame conditions are listed in Table 1. The instantaneous visible flame length fluctuates between 400 mm and 500 mm and the lift-off height was 26.3 mm, determined by CH* chemiluminescence. Both the flame length and lift-off height match well with values previously reported [17], indicating that the original flame has been reproduced reliably in the present study.

Table 1: Operational conditions for the sooting, turbulent non-premixed ethylene flame.

Exit Reynolds number	10,000
Fuel mass flow	10.4 g/min
Co-flow air mass flow	320 g/min
Fuel temperature	298 ± 2 K
Ambient temperature	294 ± 2 K
Mean fuel jet velocity	44 m/s
Lift off height	26.3 mm*
Power	8.7 kW
Flame length	~ 450 mm

DLR flame reported a lifted height of 26 mm, as determined by OH chemiluminescence [17] and 22.3 mm by OH-LIF [21].

2.2 Temperature measurements with nTLAF

In TLAF measurements, the gas phase flame temperature is derived from the intensity ratio between the two laser-induced fluorescence (LIF) signals of the tracer (e.g. atomic indium) excited from two different lower states to a common upper state. The gas temperature, T, can be calculated using the following equation,

$$T = \frac{\Delta E_{10}/k}{\ln\left(\frac{S_{21}}{S_{20}}\right) - \ln\left(\frac{F_{21}(E_{02})}{F_{20}(E_{12})}\right) + C_t}. \qquad (1)$$

Here the subscripts *0* and *1* denote the two lower electronic energy levels while *2* denote the upper energy level. S is the collected LIF signal intensity, E is the laser spectral power density, F expresses the function of LIF signal as laser power. ΔE_{10} is the difference in energy between electronic levels, and k is the Boltzmann constant. The system-dependent dimensionless calibration constant, C_t, is dependent on a number of experimental factors such as solid angle of signal collection and collection efficiency of detector. The value of C_t needs to be experimentally determined through a calibration process, which is generally performed in a particle-free steady flame, where the temperature can be measured with a thermocouple.

For the nTLAF measurement, two Nd:YAG pumped dye lasers (Quantel, TDL 90) were employed to produce laser beams centred at 410.18 nm (the Stokes beam) and 451.13 nm (the anti-Stokes beam) to excite seeded indium [32]. Indium nanoparticles was seeded into the flame with an in-house laser ablation system [33, 34]. The nanoparticles undergo thermal decomposition within the flame to release indium atoms. The excitation laser pulse energies were kept at 2.5 mJ and 3 mJ, respectively, which are in the non-linear excitation regime. The two laser beams with a ~ 120 ns temporal separation were first combined using a dichroic mirror and then focused into a laser sheet using a telescope, which results in an interrogation region with a thickness of ~ 0.4 mm and a height of ~ 10 mm. The vertical energy profile of laser sheets was recorded with a CCD camera (MegaPlus II, ES 4020) and used for the reference laser power to derive temperature. The

schematic diagram of the experimental set up for the combined nTLAF and TiRe-LII system is shown in Fig. 1.

Laser-induced fluorescence (LIF) of indium was imaged using two intensified CCD (ICCD) cameras (Princeton Instruments, PM4-1024f) both with a constant gate width of 30 ns and mounted with an image-splitter (TwinCam, Cairn). Both camera gate widths cover the laser pulse. The image-splitter was mounted with a common Nikon f/1.4 lens (f = 50 mm) for collection of the two LIF signals and a long-pass dichroic beam-splitter (DMLP425, Thorlabs) for separation of the two LIF signals. This arrangement avoids any influence of differential beam-steering on signal collection, unlike early work [18, 24]. The in-plane spatial resolution was 67×67 μm^2. The linearity response of both cameras has an R-squared value of > 0.99 for over 50% of their full dynamic range. Two customized narrow band-pass filters (Alluxa), which are centred at 451.4 nm (FWHM = 1.32 nm) and 410.4 nm (FWHM = 1.08 nm), respectively, were employed for fluorescence signals collection and spectral interference suppression, i.e. the LII signals, as well as fluorescence of PAHs, which are all induced by the TLAF beams [35]. Both of the narrow band-pass filters have a peak transmission of 95% and a high specified optical density (OD) of ~ 6.0 at the excitation laser wavelengths to suppress laser elastic light scattering (ELS) signals from the soot particles. These narrow-band filters increase both the precision and the accuracy of the measurement [35]. In addition, a reduction in the laser fluence for the present nTLAF measurements over previous configurations reduces the uncertainty due to the presence of the spectral interferences, which has been reported previously to be 10 K at a location where the f_v is 1.2 ppm [34]. With the current experimental setup, it was found that the temperature measurement has a single shot precision of 120 K in a laminar sooting flame with a peak f_v of ~ 7 ppm. This uncertainty is conservative in the present turbulent flame given the lower soot loading. The collection angle was verified to achieve uniform collection efficiency in the field of view in the present study. For each flame height, 499 instantaneous shots were acquired. The acquired images were then spatially matched and corrected for both dark charge and the laser sheet energy profile on a row-by-row basis.

A soot-free premixed ethylene/air flame burning on a Santoro-type burner was employed for the calibration of the nTLAF system, using the approach adopted previously [32]. The chosen flame relied on previous studies that showed that the calibration constants are insensitive to fuel composition and flame conditions, including temperature [32, 35]. The burner consists of two concentric brass tubes of 11 mm and 98 mm inner diameter. Gaseous fuel was injected through the central tube, while air was passed through the annular co-flow passage. The central fuel tube extends 4 mm above the surface of the annular air co-flow tube. The flow rates were 0.53 L/min for the C_2H_4 fuel, 3.91 L/min and 127.7 L/min for the premixed air and co-flow air stream, respectively. The flame temperature was measured along the centerline of the flame through the height of the laser sheets using an R-type Pt/Pt-Rh 13% thermocouple with a wire diameter of 75 μm (Omega, P13R-003). Radiation heat loss correction of the thermocouple reading was applied to account for radiation loss from the thermocouple bead to the surrounding gas. This correction involves an estimation of the energy balance between the energy received via conduction from the gas and that lost via radiation from the thermocouple bead. A correction of 61 K was added to the raw thermocouple measurement to correct for radiation heat loss. The agreements of the most-probable values and PDFs between TLAF and CARS shown in Section 3.2 suggest that this is a reasonable correction.
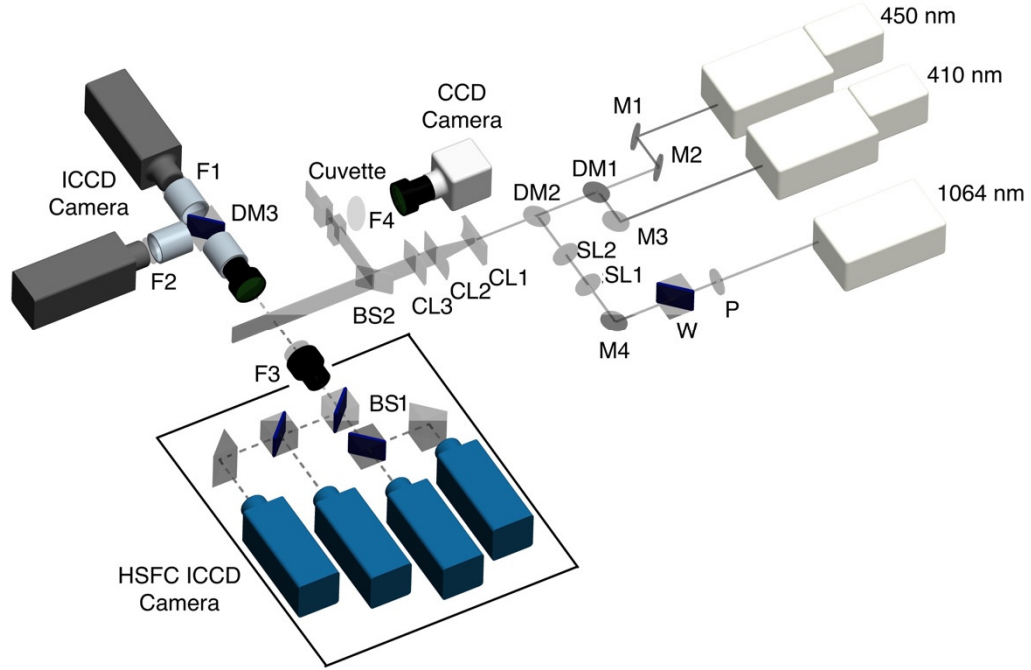
Figure 1: Schematic diagram of the experimental setup for the combined nTLAF and TiRe-LII measurements. M, mirror; DM, dichroic beam-splitter; W, half-wave plate; P, Glan-laser polarizer; CL, cylindrical lens; SL, spherical lens; F, band-pass filter; BS, prism beam splitter.

2.3 Soot volume fraction and primary particle diameter measurements with TiRe-LII

Soot volume fraction and matured primary particle diameter were measured with the TiRe-LII technique described previously [34], while primary particle number density was derived from the values of these two measured parameters by $N_p = f_v/(4/3\pi \cdot d_p^3)$. Soot particles were heated with a fundamental output (1064 nm) from a Nd:YAG laser (Quantel, Brilliant B) formed into a laser sheet of ~ 0.6 mm thickness and co-aligned with the nTLAF laser sheets. This thickness is determined by the sheet-formation optics system which is also used for the two nTLAF beams. The 1064 nm laser beam was firstly expanded (1:2) with two spherical lenses and then passes through an iris and a rectangular aperture to select the central part of the beam. The height of the laser sheet at the detection volume was ~ 30 mm, although only the LII image from the uniform central part (~ 10 mm) was selected for the following data analysis. The laser fluence was kept at ~ 0.30 J/cm^2 to ensure that the LII signal is independent of the excitation laser fluence variation without generating significant soot sublimation [36]. Four sequential LII images were collected using four ICCD camera heads (HSFC Pro, PCO) mounted with a 435 ± 20 nm interference filter (Semrock, Brightline FF02-435/40). The gate width of four cameras were all kept at 30 ns and were delayed at 0, 60, 120 and 180 ns relative to the start of the laser pulse. The in-plane spatial resolution of each camera images was 85×85 μm^2.

The prompt LII signal was used to determine f_v and was calibrated by performing laser beam extinction measurements in a steady ethylene/air non-premixed flame burned on the Santoro-type

burner. The flow rate of ethylene through the central tube was kept at 0.175 L/min and the flow rate of the co-flow air was 136.1 L/min, resulting in a flame length of 64 mm and a co-flow velocity of 0.3 m/s. A continuous wave laser at 1064 nm was used for the extinction measurement, which were performed at various heights to reduce the influence of primary particle variation through the flame on the calibration. A value of $K_e = 5.66$ was chosen for the dimensionless extinction coefficient to determine soot volume fraction [36].

The value of d_p was evaluated from the four sequential LII images by comparing the ratios of the collected signals with predictive ratios from a LII model [34, 37]. In this model, the soot particles are assumed to be non-aggregated (soot particles are aggregated in the flame) and the soot particles size to have a mono-disperse size distribution. This assumption results in an overestimation of the absolute d_p values, by up to a factor of 2 according to our previous assessments in premixed ethylene/air sooting flames and studies from other groups [26, 38, 39]. This model was used to calculate theoretical values of intensity ratio between four collected signals for d_p between 5 and 100 nm with a 5 nm step. A constant gas temperature of 1800 K was assumed in the model. The uncertainty associated with temperature variation is ~ 10% in the present study, similar to previous findings [40]. The precision of the d_p measurement is ~ 20%, as assessed in a laminar sooting flame. While the absolute accuracy of the current TiRe-LII technique is limited, the relatively high precision of the d_p measurements allows good resolution of the spatial changes to d_p in the flame.

3. Results and discussion

3.1 Images of temperature, soot volume fraction and primary particle diameter

Figure 2 presents a collage of images of flame temperature, soot volume fraction and primary particle diameter, all averaged over 499 shots, with the corresponding root-mean-square (RMS), and an instantaneous counterpart. Images were collected at 15 heights above the burner to provide data in all key regions of the flame. Mean temperature data in the present work were calculated in two alternative ways to account for the minimum detection threshold of ~ 800 K in the nTLAF method, which is due to the temperature sensitivity of the seeded indium [41, 42] or to the lack of indium LIF signal in some locations due to insufficient seeding or oxidation of indium atoms in the flame. In one method, the averaged flame temperature is calculated assuming that the temperature of any data point for which no temperature measurement was obtained is ambient, i.e. 300 K, denoted $T_{<800K=300K}$. The second method removes such measurements, which corresponds to a conditional measurement, denoted $T_{>800K}$. These two measurements can be considered as the lower and upper bounds of the mean temperature, respectively, to provide confidence in the mean data where the two methods agree. In addition, even in some regions where temperature > 800 K, there are some local regions where atomic indium may not be available due to oxidation. The significance of the minimum detection threshold of ~ 800 K is assessed by reporting the fraction of the data set for which good data are obtained, termed $F_{good\ data}$, i.e. the fraction of the temperature data that is > 800 K.

Slight asymmetry was found in all mean images of T, f_v and d_p, which have higher value on the left side (laser entrance) than the right side (not clearly shown in Fig. 2, see radial profiles of f_v in Fig. 5). The asymmetry persists after rotating the burner, suggesting that this asymmetry was not caused by an uneven flow distribution. Furthermore, this finding is consistent with the asymmetry in f_v reported by Köhler *et al.* [21]. This asymmetry is likely to be associated with the local laser fluence decrease when the LII laser sheet crosses the flame, which was caused by beam steering and laser attenuation due to high local f_v, and signal trapping [43, 44].

Figure 2a shows that a measurement of $T_{<800K=300K}$ is obtained in most regions of the flame, except near to the axis and with a flame height (h) between 40 and 120 mm. Figure 2b shows that the soot starts to become detectable at a height of ~ 120 mm and extends to the flame tip ~ 420 mm, similar to the temperature distribution detected with nTLAF. In the middle height regions of the flame, i.e. between 200 and 350 mm, the radial width of measured temperature is wider than f_v and d_p, indicating nTLAF is capable of measuring temperature on either side of soot sheets. The instantaneous images in Figs. 2d and 2e confirm that the region of measureable temperature is instantaneously over a wider region than that of the soot, which is important for reliable joint PDFs. The temperature RMS image shows that the radial fluctuations are small for $h < 230$ mm and increase towards the flame tip, consistent with single-shot images shown in Fig. 2d.

The peak f_v in the mean image is ~ 0.52 and ~ 4.7 ppm at $h = 310$ mm in the instantaneous image, comparing with corresponding values of 0.54 ppm and 4.5 ppm at $h = 300$ mm reported by Köhler *et al.* [21]. The average values of f_v (Fig. 2b) are an order of magnitude lower than the instantaneous values (Fig. 2d), consistent with previous measurements [5, 45], which is due to both the highly intermittent nature of the soot distributions [19] and the isolated, highly-wrinkled structure of the soot distribution. In the burnout region of the flame, i.e. $h \sim 375$ mm, although the mean f_v decays from the peak of 0.52 ppm at $h = 310$ mm, the instantaneous f_v can still reach a maximum of 4.6 ppm, indicating the number of occurrence of detectable f_v is less than at the lower flame positions, consistent with findings from previous measurements [17, 19]. The dimension of the soot sheets was found to be larger in the burnout region than that of lower flame locations, also consistent with the previous measurements [17, 19] . It should also be noted that f_v is detectable at $h \sim 425$ mm in the mean image, while T is not detectable at this height. This may be because: 1) nTLAF measurements were biased since indium was consumed and temperature is relatively cold in this region; and 2) the fluctuation of f_v is much larger than that of T due to rapid oxidation of soot. The f_v RMS distribution has a relatively high amplitude further from the flame centreline than does the f_v mean distribution, also indicating the highly fluctuating nature of the soot sheets in turbulent flames, both in magnitude and spatial distribution. The comparison of instantaneous T and f_v images (Figs. 2d and 2e) reveals that soot sheets are generally found in a temperature range between 1400 and 2000 K, on the rich side of the high temperature reaction zones, consistent with earlier measurements [7, 9, 11].

Figures 2c and 2f show that d_p grows from the outer edge of the flame at $h = 120$ mm towards the central region at downstream locations, peaks at $h = 310$ mm on the axis with an averaged value of 16 nm and ~ 80 nm in the instantaneous images, and then oxidises at the flame tip. The values of d_p are comparable with those measured by TiRe-LII in laminar ethylene diffusion flames [26, 40], in an unsteady ethylene/air premixed flame [34] and simulated results in a different ethylene turbulent diffusion flames [46]. For $h > 150$ mm, the d_p RMS image has a similar width and magnitude to the mean image, indicating the fluctuation in d_p is less than that of f_v, but larger than that of T.
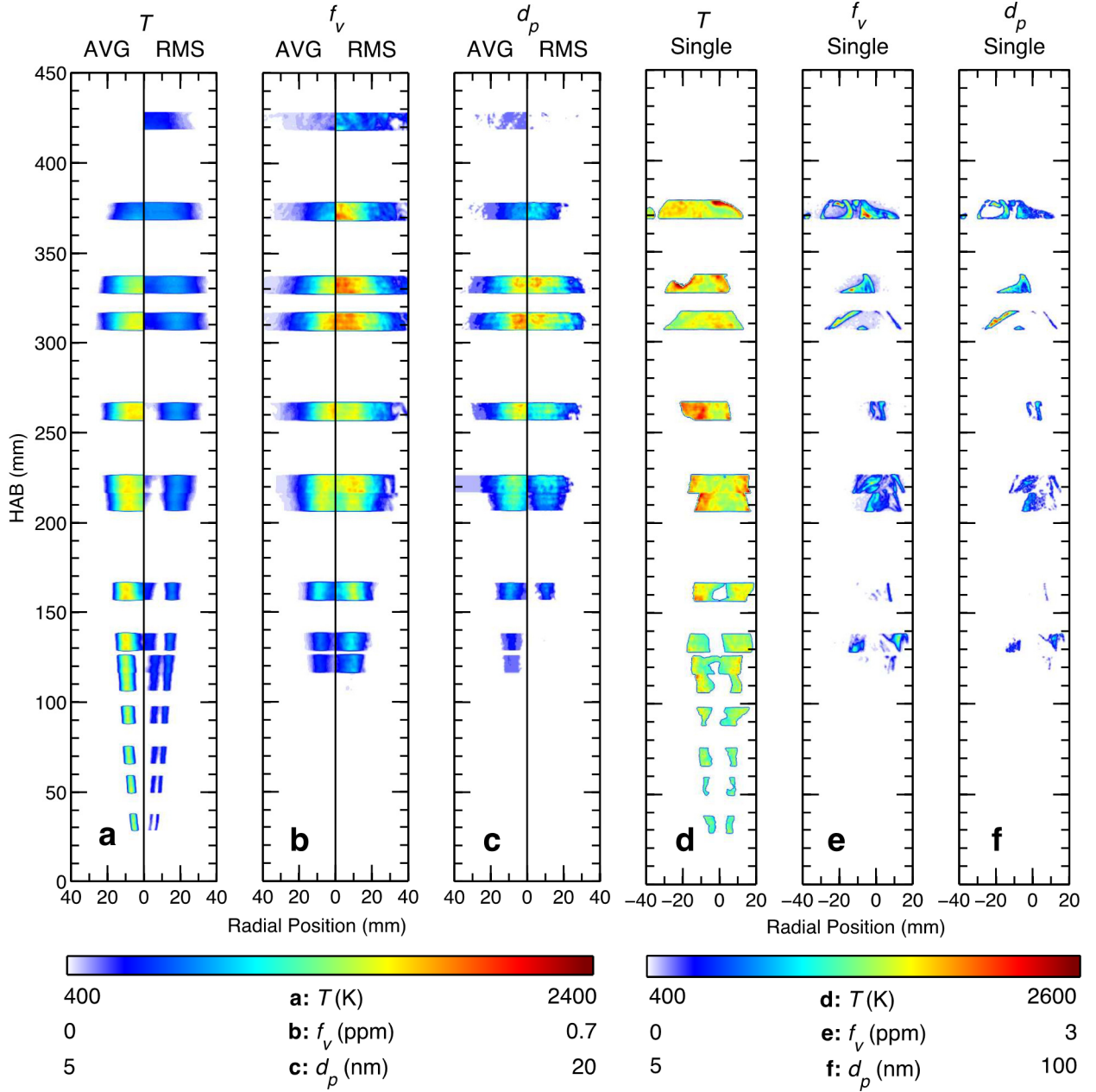
Figure 2: Pseudo colour images of: (a) the averaged flame temperature ($T_{<800K=300K}$) and corresponding RMS; (b) the averaged soot volume fraction (f_v) with a maximum $f_v = 0.52$ ppm and corresponding RMS; (c) the averaged primary soot particle diameter (d_p) and corresponding RMS; typical single-shot images of T; (d) single-shot images of f_v with a peak f_v of ~ 4.7 ppm and (e) single-shot images of d_p.

3.2 Temperature data

Figure 3 presents the PDFs of flame temperature on the axis at selected heights, together with the Gaussian fits, both for the present nTLAF measurements and for the previous CARS measurements [21]. The distributions of the CARS measurements are scaled according to the CARS results at $h = 208$ mm. The nTLAF data presented were extracted from 499 (for Figs. 3a, 3c-f) and 998 (for Figs. 4b and 4g) instantaneous image pairs, respectively, with each measurement averaged from a sub-array of adjacent pixels to increase signal-to-noise ratio in the raw LIF images. Most data are

reported from a 5 × 5 pixels array (0.33×0.33 mm^2), while some data are reported from a lower resolution of 0.4×0.4 mm^2 and a higher resolutions of 0.2×0.2 mm^2, as shown in Fig. 3e. The PDFs at measurement each location are calculated from a further array of 5 × 5 neighbouring points, i.e. each measurement location has a total sample size of either 12475 or 24950 measurement points. The corresponding spatial resolution of the CARS measurement is 2.2×0.3 mm^2 and the corresponding number of samples is 1200 shots.

The temperature distributions from the nTLAF and CARS measurements are in good agreement over the region between $158 < h < 418$ mm, as shown in Figs. 3c-g. The poor agreement for $h < 78$ mm, where the nTLAF distribution over-predicts the temperature statistics, can be explained by the high probability that the temperature is below the lower detection limit of the nTLAF technique as evident that $F_{good\ data} < 0.36$. This shows that the nTLAF measurements in these regions should be treated with caution. Figure 3h shows that $F_{good\ data}$ is larger than 0.9 over the region $158 < h < 308$ mm and is also greater than that of corresponding CARS measurements in this same region. Furthermore, while the value of $F_{good\ data}$ decreases towards the flame tip for $h > 308$ mm, the values of measured temperature are comparable with the CARS measurement except for the region very close to the flame tip ($h = 420$ mm), where $F_{good\ data}$ is 24.1% and 61.2% for nTLAF and CARS measurements, respectively.

The most probable values of measured temperature, denoted T_{mp}, are found to agree within 30 K for the nTLAF and CARS data over the range $158 < h < 418$ mm. The width of the nTLAF data distribution is slightly wider than that of the CARS data for $208 < h < 308$ mm. This is attributed to the combination of inter-pixel noise in the raw LIF images and to the variation in the laser mode from shot-to-shot. Figures 3a-g present the PDFs from the nTLAF measurements with a spatial resolution of 0.4×0.4 mm^2 (black dash line). They generally agree with the distributions from the 0.33×0.33 mm^2 resolution (black line) and eliminate the high temperature portion in the distributions. Figure 3e further presents the influence of spatial resolution on the measured temperature. It can be seen that increasing the spatial resolution, and hence lowering the signal-to-noise ratio, results both in a wider distribution of the PDF and in a higher value of T_{mp} than that from the low spatial resolution. This trend is real, because high spatial resolution is subject to increased noise in the temperature calculated from a larger number of samples, which will increase the scatter in the temperature data. The spatial resolution of 0.33×0.33 mm^2 gives generally good agreement with the CARS data, with the slightly wider distribution consistent with a slightly smaller probe value, which is the reason that this spatial resolution has been selected for further analysis.
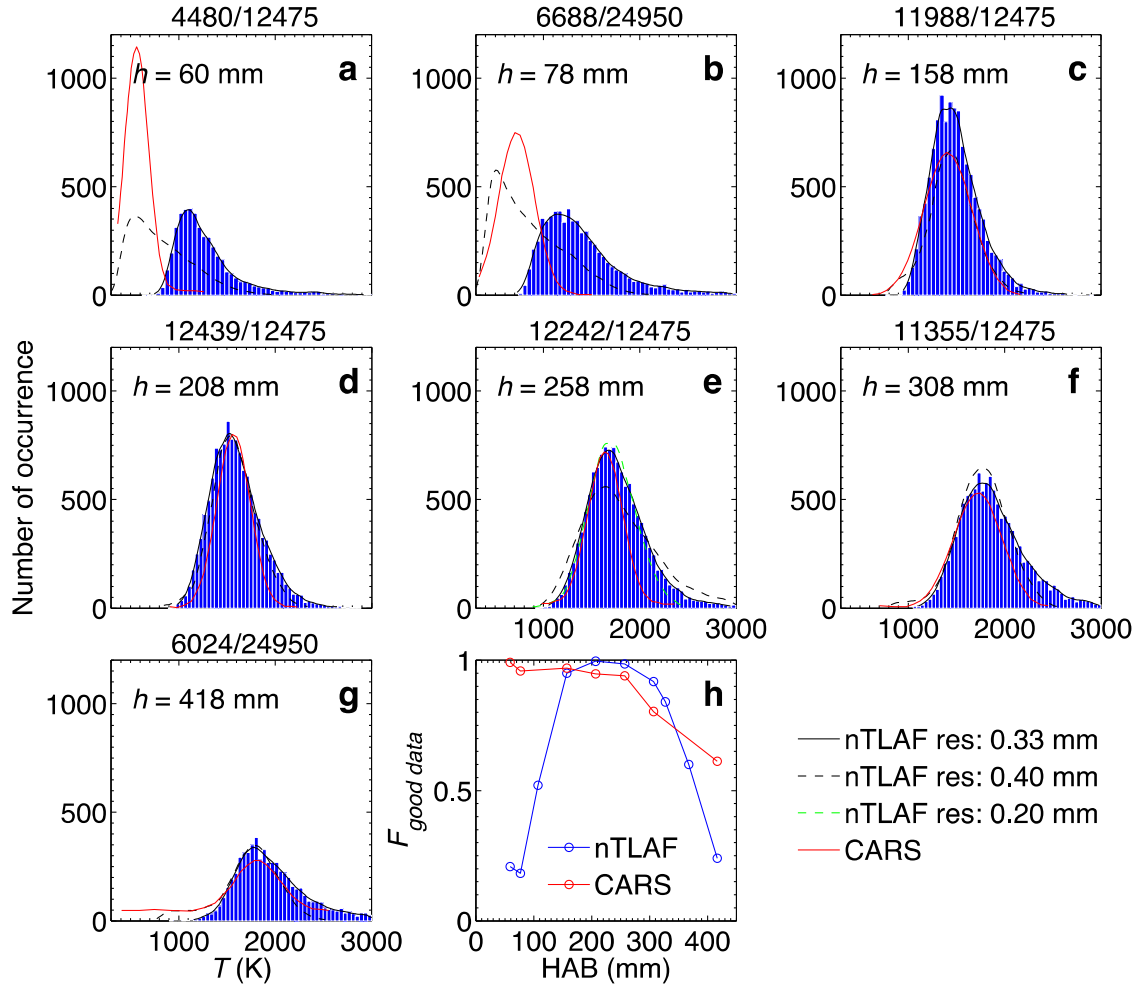
Figure 3: (a-g) Probability density functions (PDF) of instantaneous temperature at selected centreline locations. The number above each figure correspond to the number of good temperature measurements and the sample size of temperature measurements for the nTLAF measurements. Fitted curves from CARS measurement [21] are shown in red lines. Part (h) presents the axial evolution of the fraction of good temperature data, along the centreline. Part (e) presents the various fitted curves acquired from nTLAF data with different spatial resolutions to the 0.33×0.33 mm^2 reference case.

Figure 4 presents the axial and radial profiles of temperature from the nTLAF and CARS measurements [21]. As shown in Fig. 4a, both the values of $T_{<800K=300K}$ (black circles), corresponding to the lower bound of mean nTLAF temperature, and the values of $T_{>800K}$ (blue circles) yield good agreement with the CARS data in the central region of the flame ($140 < h < 300$ mm). The convergence of $T_{<800K=300K}$ with $T_{>800K}$ implies a high reliability of the statistical measurements at these location. For $150 < h < 130$ mm and $h > 300$ mm, the value of $T_{<800K=300K}$ is lower than CARS data while the value of $T_{>800K}$ is higher, which is consistent with low values of $F_{good\ data}$ there. The same trends can be found in the radial profiles. Both the good agreement between $T_{<800K=300K}$ and CARS data and the overestimation of $T_{>800K}$ compared with the CARS data for $r < 5$ mm at $h = 113$ mm show that gases below 800 K within this region are dominated by cold fuel gas. There is some disagreement between the three methods at $h = 113$ mm and $r = 9$ mm, where $T_{<800K=300K}$ matches well with $T_{>800K}$, but both nTLAF results are lower than T_{mp} and T_{mean} of CARS data by 186 K and 400 K, respectively. Towards the outer region, i.e.

$r > 9$ mm, the $T_{>800K}$ and $T_{<800K=300K}$ increasingly deviate from each other again as expected, due to the increasing significance of the temperatures below 800 K caused by the periodic entrainment of cold ambient air. While no comparisons with the CARS data are available here, these upper and lower-bounds to the data are nevertheless both useful. In addition, it can be expected that the upper-bound approaches the unconditional value most closely near to the axis, while the lower bound measurement will approach the unconditional value more closely as the radial distance from the axis is increased.
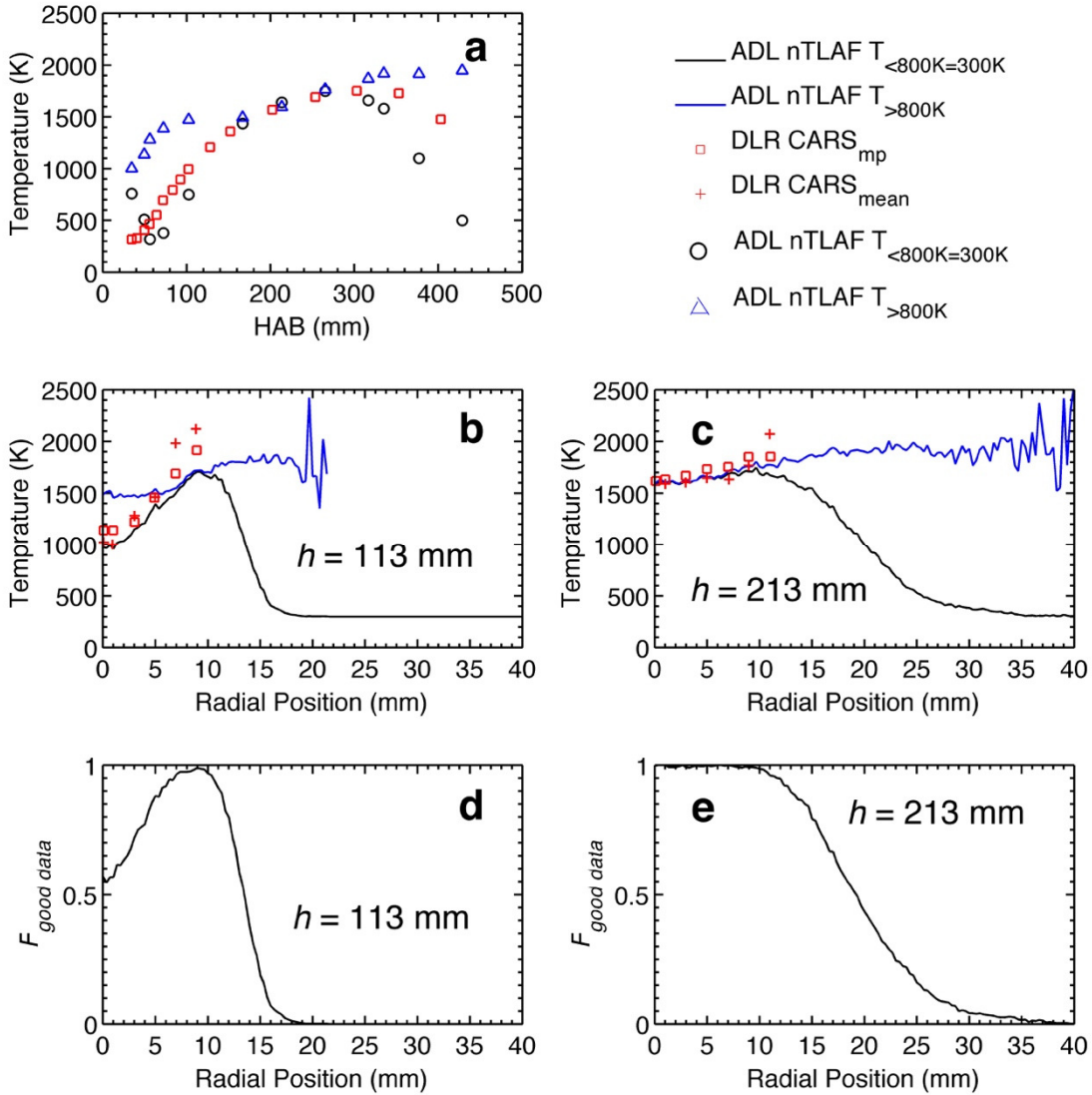

Figure 4: Comparison of the mean nTLAF data (0.33 mm resolution) obtained from 499 images (here denoted as ADL nTLAF) with CARS data obtained from 1200 shots (here denoted as DLR CARS). (a) Axial profiles; radial profiles at (b) $h = 113$ mm and (c) $h = 213$ mm. The averaged lower-bound temperature ($T_{<800K=300K}$) from nTLAF data is shown in black lines, while the upper-bound conditional mean temperature ($T_{>800K}$) is shown in blue lines. The most probable (T_{mp}) and mean (T_{mean}) temperature from CARS measurements [21] are shown in red squares and crosses, respectively.

3.3 Soot volume fraction and primary particle diameter

Figures 5a and 5b present comparisons of the axial profiles of measured f_v and d_p from the present work with previous values of the measured f_v [21]. The profiles from the present work is obtained by averaging over 499 shots, while the previous data is averaged over 1000 shots. The two measured axial profiles of f_v are in good agreement with each other, with a maximum difference of $\sim 13\%$ for $200 < h < 300$ mm, and an agreement of within 5% for the other positions. For $h < 150$ mm along the axis, d_p is below the detection limit of 5 nm. The measured d_p starts to grow with f_v and peaks at $h = 310$ mm on the axis with an averaged value of 16 nm. The mean d_p then decreases towards the flame tip at a rate faster than it grows, similar to the f_v trend.

The radial profile of f_v at four heights are shown in Fig. 5c and compared with the previous measurements [17]. The profiles show that the peak value is away from the axis for $h \leq 160$ mm and on the axis at more downstream locations. Very good agreement is found between the two sets of the f_v measurements, although the width of the present f_v profile is somewhat less than the previous one [17], as shown in Fig. 5c. Since the centerline f_v profiles agree well, this difference in width is unlikely to be due to misalignment of the laser sheet with the axis of the flame. It is possible that slight difference in the environment, such as the influence of the ambient, may play a role, but the reason for this discrepancy is still unclear. Distinct asymmetry can be seen for $h \geq 120$ mm in both f_v profiles, which is attributable to a reduction in the laser fluence with propagation distance by the high f_v and/or by the influence of beam steering due to turbulence.
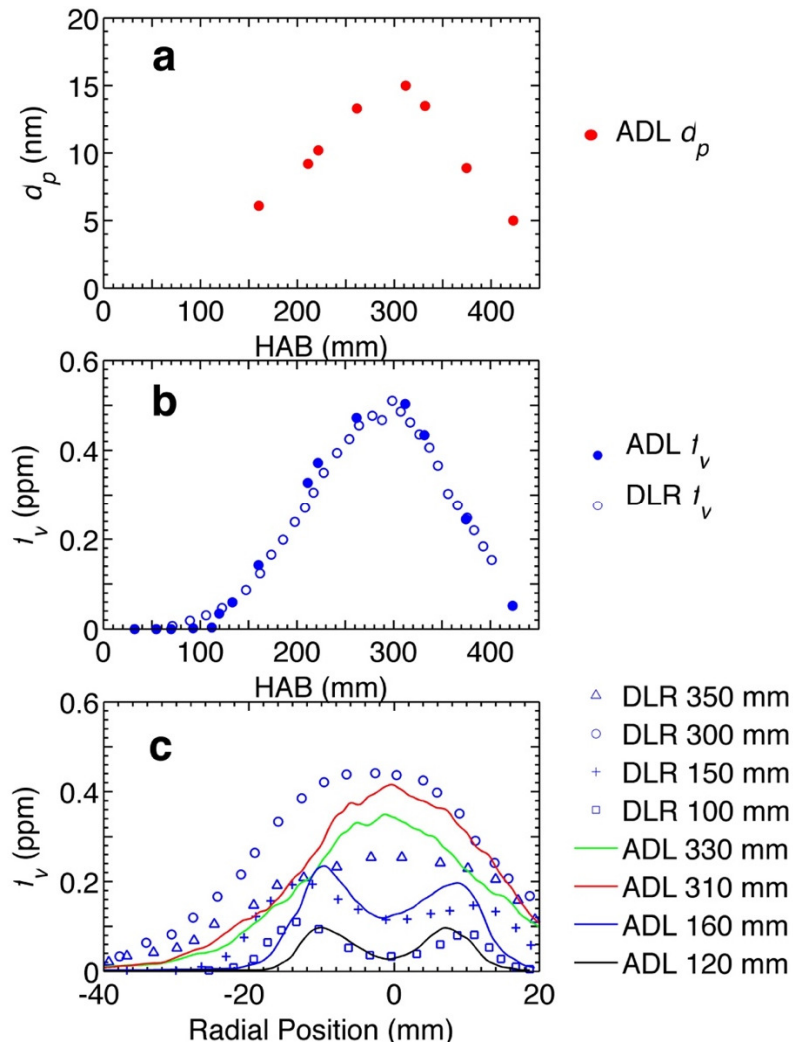
Figure 5: (a) Mean axial data of measured d_p from the present study. (b) Comparison of the present and previously measured [17] mean axial data of f_v. (c) Comparison of the present and previously measured [17] mean radial profiles of f_v at selected heights. The measurements from the present study are denoted as ADL and from the previous study [17] are denoted as DLR.

3.4 Radial profiles of temperature, soot volume fraction and primary particle diameter

Figure 6 presents the mean and RMS radial profiles of T, f_v, d_p measured at six axial locations. The presented mean temperature profiles are calculated by assuming that any data points for which no temperature measurement was obtained is ambient, i.e. $T_{<800K=300K}$. The radial profiles of T at the first three flame heights ($x/d = 67$, 80 and 105, where x is the distance along the flame axis and d is the inner diameter of the burner exit nozzle) show a trend of increasing with increasing radial distance from the centerline, followed by a decrease towards the flame edge. For these three axial locations, both the rates of increase and decrease are most pronounced at the base of the flame, i.e. at $x/d = 67$. The corresponding radial profiles of f_v and d_p follow the same trend. While the RMS values for T and d_p measurements are lower or comparable to the mean values, the RMS values for f_v are always higher than the mean values, consistent with a highly intermittent distribution of f_v. At $x/d = 187$, the RMS values of f_v are more than two times larger than the mean values, indicating high intermittency as well as rapid soot oxidation in these regions.
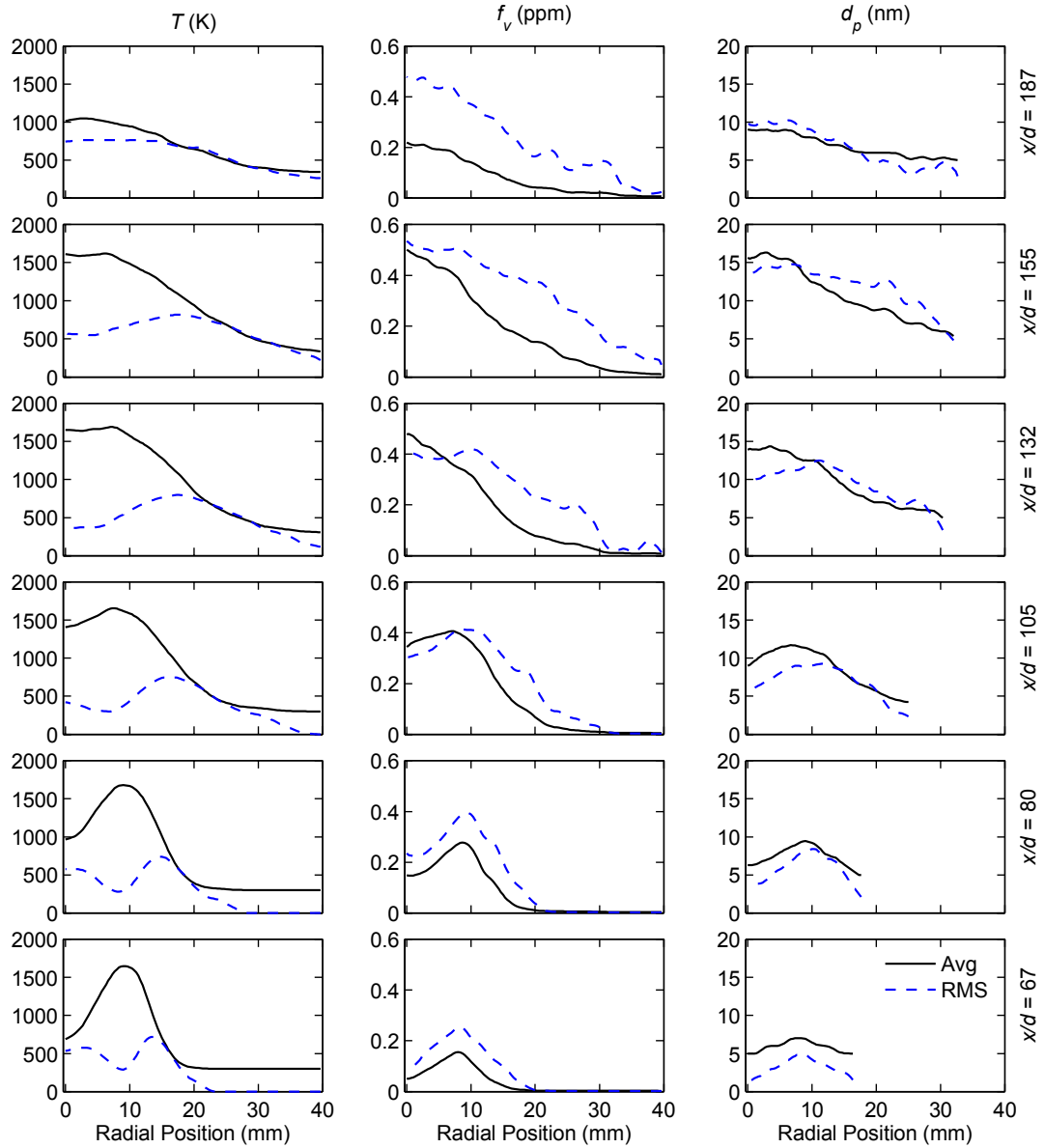
Figure 6: Radial profiles of the mean and RMS of temperature ($T_{<800K=300K}$), soot volume fraction and primary particle diameter at various axial (x/d) locations.

3.5 Joint statistics of T, f_v, d_p and N_p

Three radial locations at five flame heights have been selected to analyse the instantaneous correlations between T, f_v, d_p and N_p. The three radial locations at each flame height are on the centreline and at 50% and 90% of the half width of the soot zone (denoted as W_f), respectively. In addition, they are all on the laser entrance (i.e. the left) side of the flame. The soot zone width is determined from the contour of f_v. The position at which the joint statistics were obtained relative to the mean f_v image is illustrated by the black dots in Fig. 7.
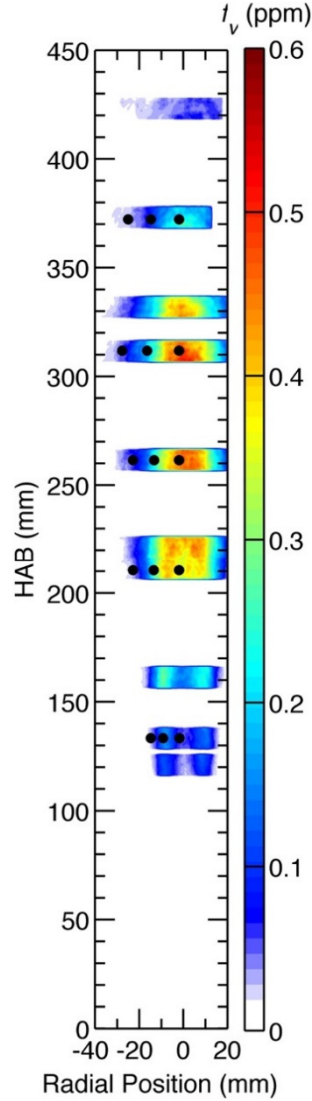
Figure 7: Pseudo colour images of the averaged soot volume fraction overlayed with selected positions for the joint PDFs presented below (*black dots*).

Figure 8 presents the joint PDFs between T and f_v. The pseudo colour contours represent the probability, while the outer blue line defines data within plus or minus two times of the standard deviation of the set. These statistics from the instantaneous data show that a strong but not circular correlation distribution exists between T and f_v at all chosen locations. The distributions of the PDFs show a strong dependence on axial distance, while the dependence on radial distance is much stronger near to the base of the flame than at the tip. This is broadly consistent with previous findings reported by Mahmoud *et al.* [18], Coppalle *et al.* [7] and Shaddix *et al.* [10], although the present work finds a stronger dependence on radial distance near to the base of the flame. On the axis of the flame, soot is typically formed at gas temperatures between 1400 and 2000 K with the peak f_v found between 1550 and 1750 K. These gas temperatures are higher than previously reported values of soot temperature between 1500 and 1700 K [7] and between 1350 and 1550 K [10], which were obtained at different flame conditions and with different measurement techniques. The range of f_v is very large, varying over some two orders of magnitude, similar to earlier findings [7, 10]. The distribution of T along the axis is widest near to the middle of the flame where f_v peaks,

while the width of this peak also increases with radial distance, particularly at upstream locations, i.e. near to the base of the flame. This is slightly different from the trends reported previously, in which it was found that the joint PDF between T and f_v is mainly dependent on the axial distance and only very weakly depend on radial location [18]. That is, the nature of the distribution depends strongly on the position within the flame, so that no simple relationship between T and f_v can be applied generally throughout the flame.

Along the centreline of the flame, the most probable f_v is ~ 0.02 ppm, at $x/d = 67$, increasing to ~ 0.1 ppm for $105 < x/d < 132$ mm and then decreasing slightly to 0.08 ppm at $x/d = 155$. At the flame tip, $x/d = 187$, the most probable f_v decreases to ~ 0.02 ppm. The most probable corresponding temperature, which increases with axial distance and then slightly decrease at the flame tip, are 1420 K, 1500 K, 1640 K, 1900 K and 1850 K respectively. These trends of most probable T and f_v are with good qualitative agreement with the measurement of Shaddix *et al.* [10] at $x/d = 140$ and $x/d = 200$. Although their most probable values of f_v are somewhat higher at ~ 0.4 ppm for $x/d = 140$ and 0.1 ppm for $x/d = 200$. However, these differences are not inconsistent given the larger size of their flame, their use of a pilot to achieve an attached flame instead of the present lifted flame and different measurement techniques. In Fig. 8, similar trends in the most probable values of T and f_v can be found at $R = 0.5W_f$ with a slightly smaller change in the most probable f_v with the axial distance. At the flame edge of $R = 0.9W_f$, neither the most probable values of T nor f_v change much. From the flame centreline to $R = 0.5W_f$, both the value of the most probable f_v and the number of events with high f_v decrease, while the most probable value of T increases, consistent with an increasing probability of oxidation through the high temperature region. It is worth noting that, the most probable values of f_v in the joint PDFs are some four to five times lower than the corresponding mean values of $f_v = 0.45$ ppm at $x/d = 132$. They are also lower at $x/d = 105$ and 155 by factors of about three and five, respectively. This is found to be consistent not only with the large value of RMS of f_v shown in Fig. 2b, but also with the very large difference between instantaneous and mean values.
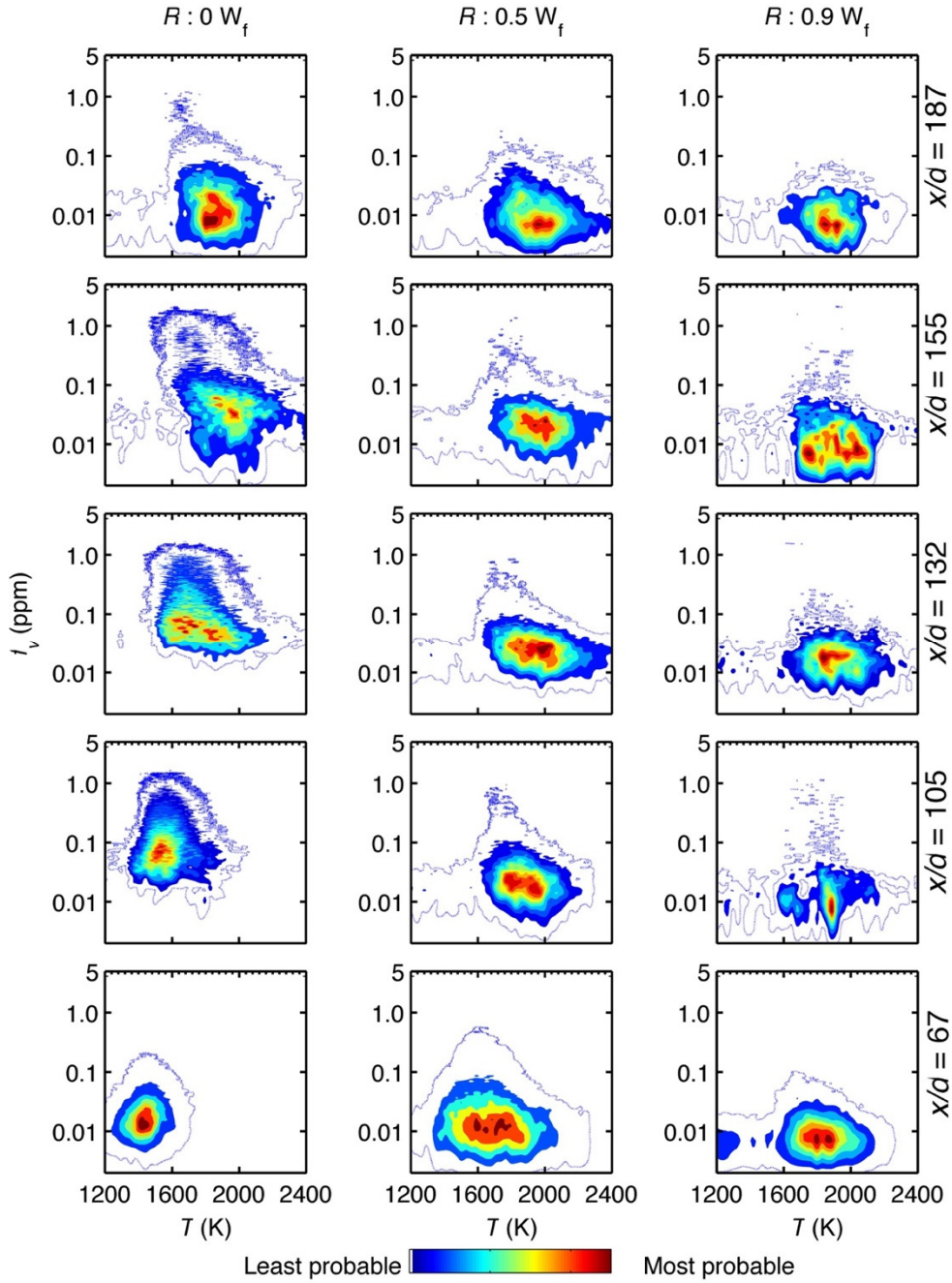
Figure 8: Joint PDFs of T and f_v at selected axial and radial locations (see Fig. 7 for positions). Statistics were calculated from 499 image sets over an area of 5 (radial) × 3 (axial) mm², i.e. 15 × 9 neighbouring points, each binned from 5 × 5 pixels.

Figure 9 presents the joint PDFs between d_p and f_v. A strong correlation exists between d_p and f_v at all locations, which is broadly consistent at all axial and radial locations. The trend is clearly shown by comparing the joint PDFs data with a reference curve shown in all subfigures. The reference curve is fitted for the joint PDF data at $x/d = 105$ and $R = 0$ W_f based on a power-law function. For all locations, the most probable value of d_p is between 8 and 18 nm, while the corresponding most probable f_v is between 0.1 and 0.5 ppm. Large primary soot particles with $d_p > 30$ nm mostly correspond to $f_v > 1$ ppm. There is a slight trend of data being below the reference power-law curve near to the edge of the flame, showing that diameter relative to volume fraction decreases with radial distance. This decrease is associated with an increased significance

- 19 -

of oxidation, although more data is required to quantify the role of oxidation in this process. It is also significant that the range in the distribution of range of d_p increases with both axial and radial distance. The greater prevalence of larger particles can be deduced to be associated with the increased significance of surface growth and coagulation, although again more data are required to quantify their role. The span of d_p is much greater toward the flame tip, even though it falls closely on the power-law curve throughout. At downstream flame locations, the increase in the distribution range of d_p with axial distance is consistent with a much wider range of evolution of soot particle histories. At the centreline, both d_p and f_v grow from $x/d = 67$ to $x/d = 155$ mm and the mean value of d_p decreases slightly at the flame tip. Similar trends can be found at $R = 0.5W_f$ and $0.9W_f$. The width of d_p for a given f_v value decreases radially from the centreline to the flame edge, while the maximum d_p increases radially for a given height.
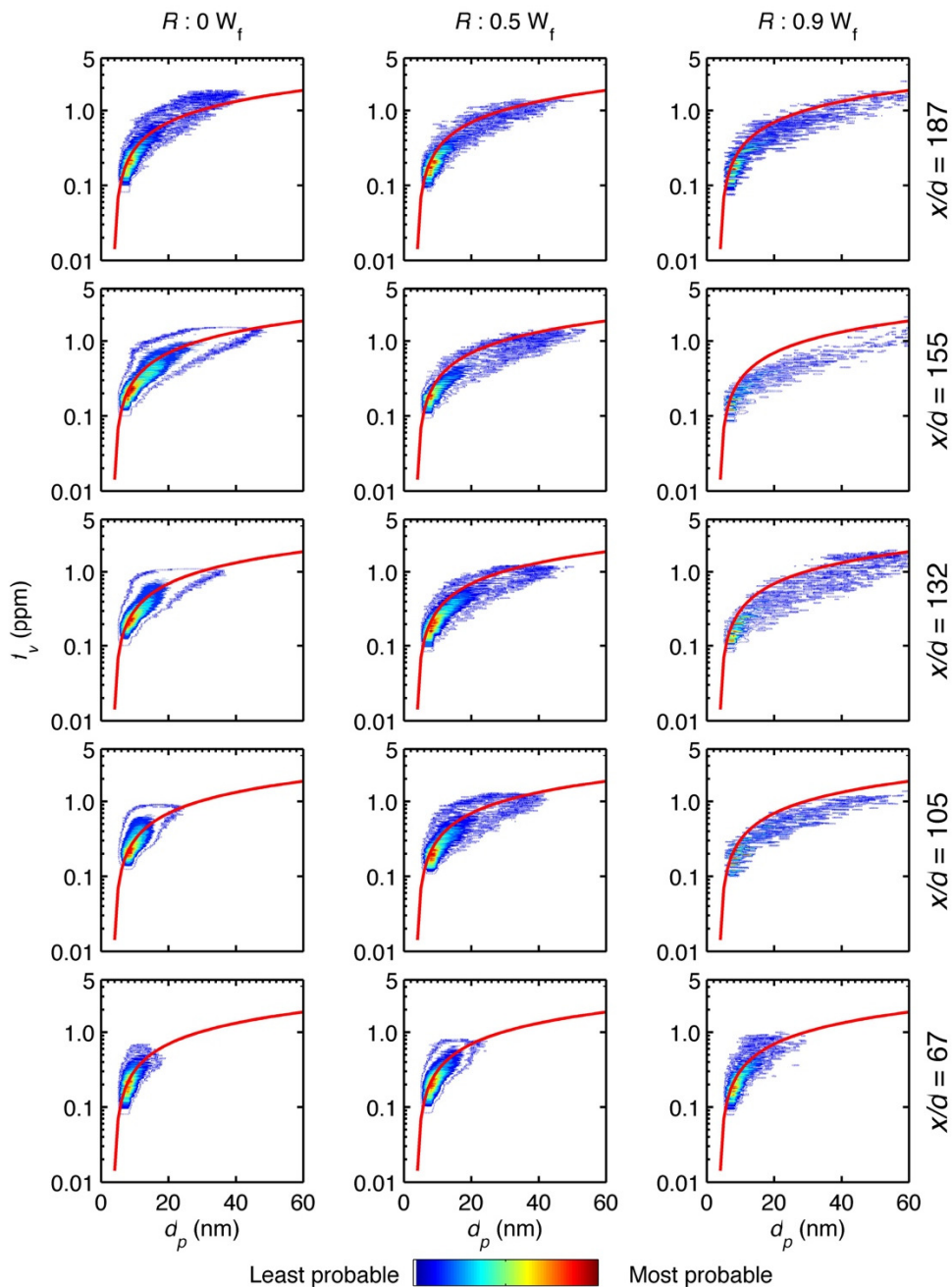
Figure 9: Joint PDFs of d_p and f_v at selected axial and radial locations. Statistics were calculated from 499 image-sets over an area of 5 (radial) $\times$ 3 (axial) mm^2, i.e. 15 $\times$ 9 neighbouring points (with each point binned from 5 $\times$ 5 pixels). The red line corresponds to a power-law function fitted from experimental data at $x/d = 105$ and $R = 0$ W_f.

Figure 10 presents the joint PDFs between T and d_p at selected locations, showing a strong correlation between T and d_p on the axis and near to the base of the flame. This correlation becomes weaker with an increase in both axial distance towards the tip and with radial distance toward the flame edge. That is, both the value and the range of the most probable d_p increases with axial and radial distance. Also, the small soot particles are found at a wider range of T than the larger soot particles, which is consistent with previous finding in laminar flames [47]. At any given positions, the most probable T is almost independent of d_p, except near to the tip, where there is a weak trend that the larger soot particles are most likely at relatively low temperature ranges. This is consistent with the joint PDFs of T and f_v, as shown in Fig. 8. It should also be noted that soot particles of different sizes can be found at the flame edge, where f_v is small (in Fig. 8).
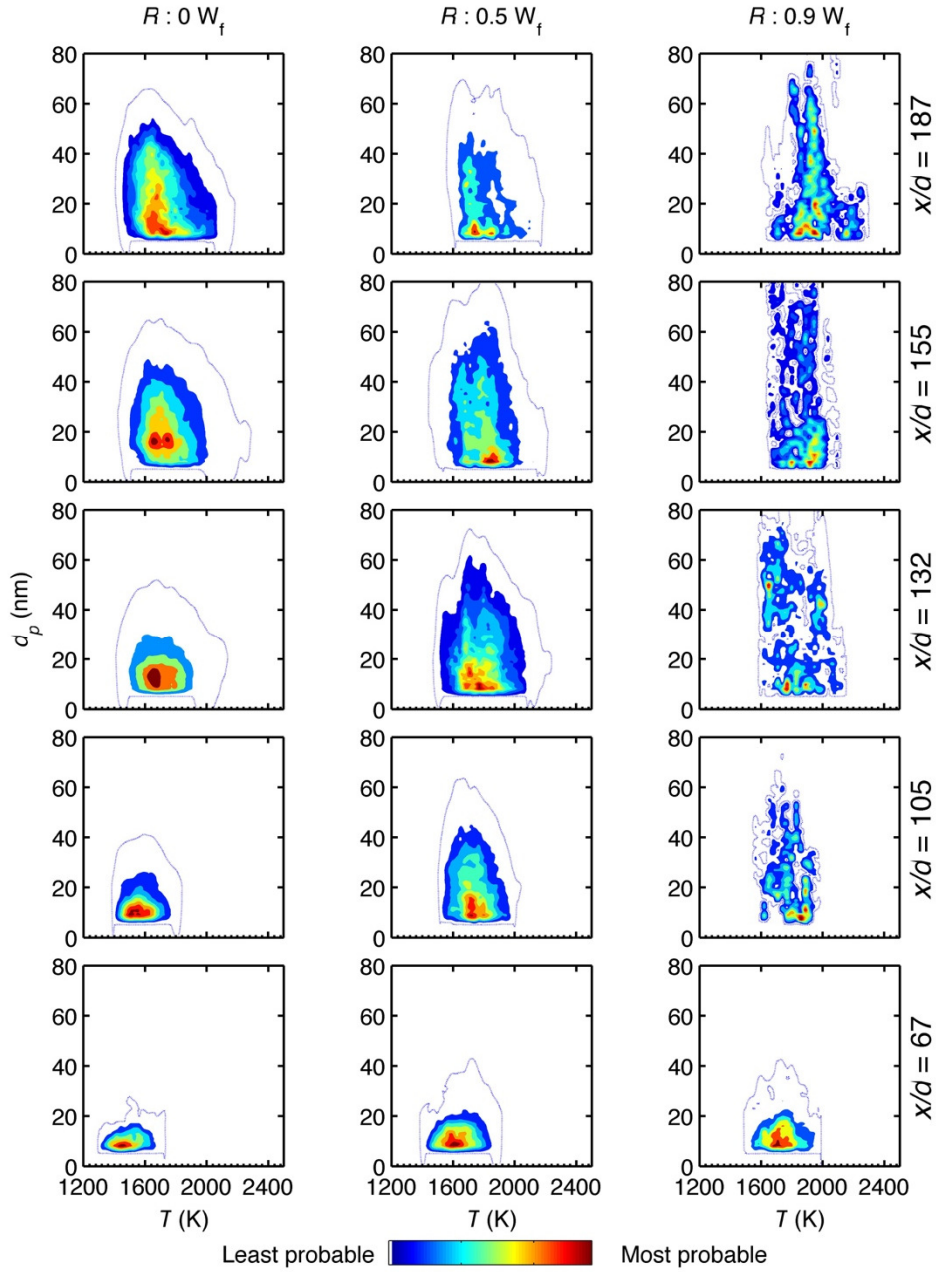
Figure 10: Joint PDFs of T and d_p at selected axial locations and radial locations derived from 499 image sets. Statistics were calculated from an area of 5 (radial) $\times$ 3 (axial) mm^2 which consists of 15 $\times$ 9 neighbouring points (each point derived from 5 $\times$ 5 pixels).

Figure 11 presents the joint PDFs between N_p and T. For all locations, the most probable N_p is between 10^{16} and 10^{18} m^{-3}, and decreases from the flame axis towards the flame edge, while the corresponding most probable T varies with flame locations. The most probable N_p increases axially from the flame base to $x/d < 132$, indicating soot inception takes places in these regions. The most probable N_p then decreases towards the flame tip, suggesting soot particle oxidation. The value of N_p reaches a maximum of 7.0×10^{17} m^{-3} at $x/d = 105$ on the flame axis. Also, the maximum value of N_p decreases from flame centre towards flame edge at all selected flame heights, while the value of most probable N_p decreases with radial distance.
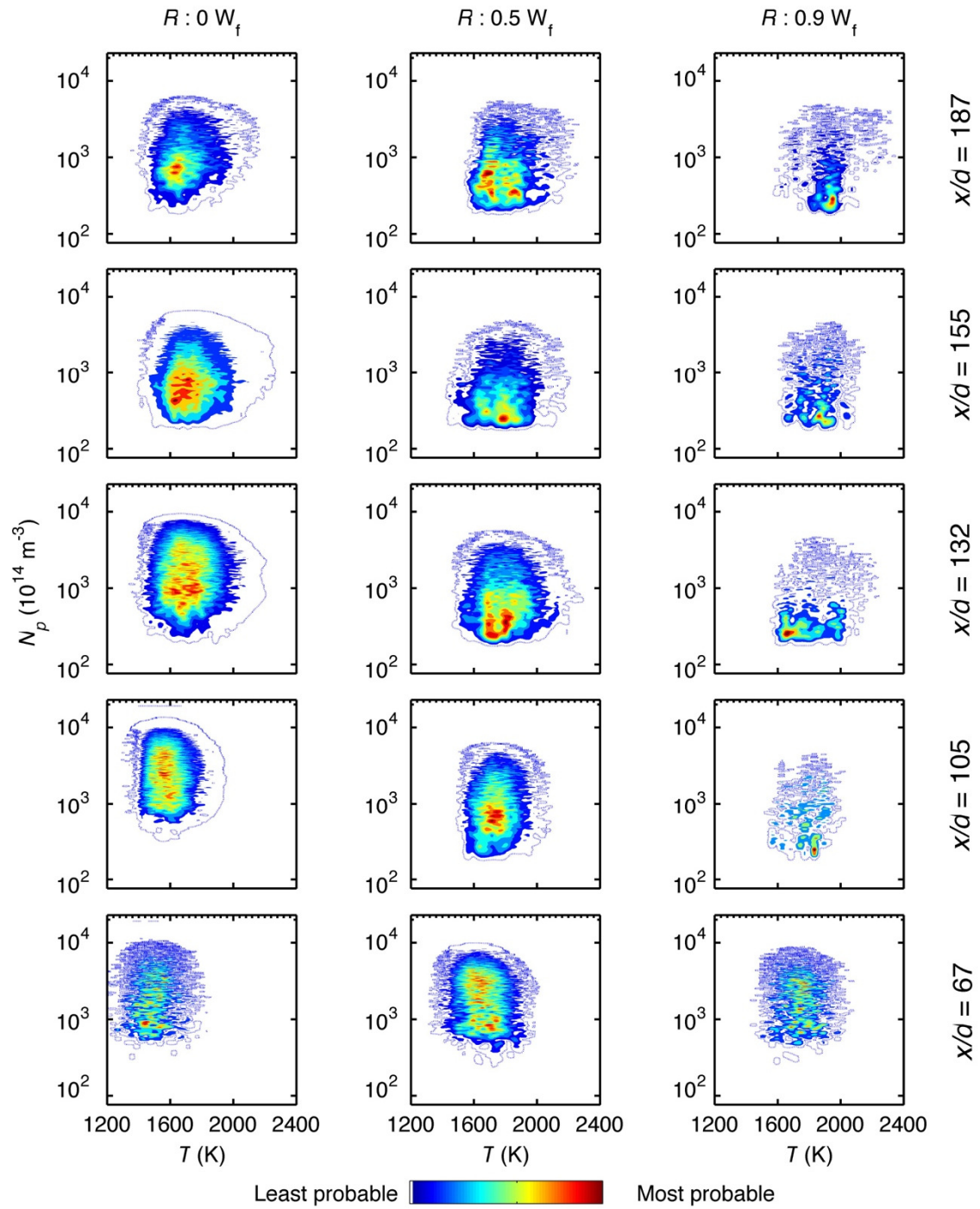
Figure 11: Joint PDFs of N_p and T at selected axial and radial locations. Statistics were calculated from 499 image-sets over an area of 5 (radial) $\times$ 3 (axial) mm^2, i.e. 15 $\times$ 9 neighbouring points (with each point binned from 5 $\times$ 5 pixels).

Figure 12 presents the joint PDFs between N_p and f_v. The value of N_p increases with the increase of f_v for $f_v < 0.4$ ppm and decreases when f_v exceeds 0.4 ppm. The latter trend may attribute to high number densities of young soot particles cause intense coagulation and agglomeration and result in a sharp decrease in number densities. This trend is also found consistent with previous

measurements in laminar flames [48]. The maximum value of N_p in all cases is $\sim 5.0 \times 10^{17}$ m^{-3} and the corresponding f_v is ~ 0.4 ppm. The joint PDFs of N_p and f_v were fitted with a power-law function, i.e. $N_p(f_v) = a \times f_v^b$. A reference power-law function, which is calculated from the PDF at $x/d = 132$ and $R = 0W_f$, was plotted against experimental data in all subfigures in Fig. 12, to identify the trend of the PDFs. Figure 13 presents the fitting coefficient, b, here denoted K_{Nf}, for selected axial and radial locations. For $f_v < 0.4$ ppm, it can be found that the value of K_{Nf} decreases with flame heights of $x/d \leq 155$ and then increases towards the flame tip, as shown in Fig. 13a. For $f_v > 0.4$ ppm, the value of K_{Nf} increases with flame heights at all three selected radial locations, i.e. the decrease in N_p with the increase of f_v decreases at downstream locations when compared to upstream locations, as shown in Fig. 13b. The decrease in N_p with the increase in d_p increases from the centreline of the flame towards the flame edge, as shown in Figs. 13c and 13d.
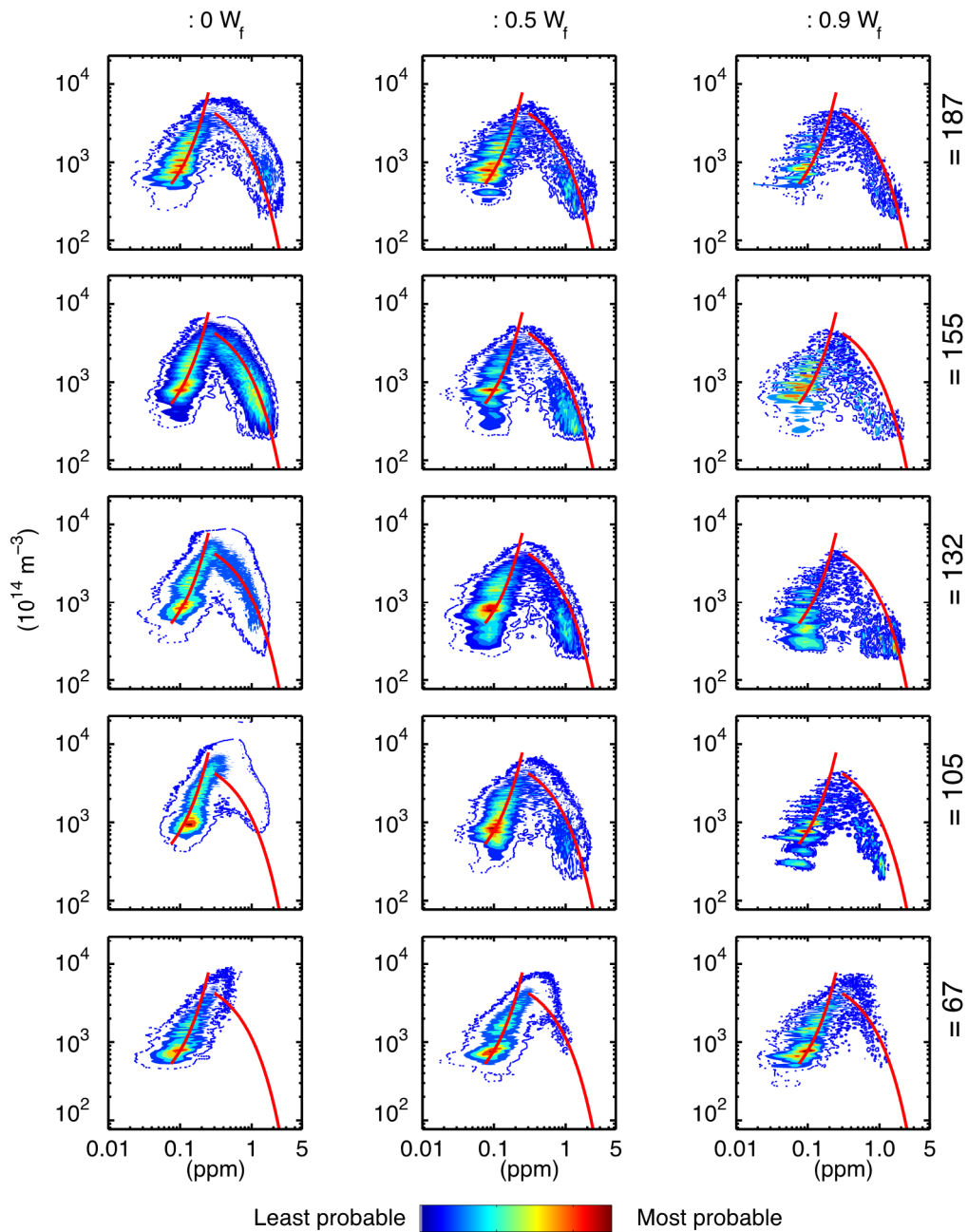
Figure 12: Joint PDFs of N_p and f_v at selected axial and radial locations. Statistics were calculated from 499 image-sets over an area of 5 (radial) × 3 (axial) mm², i.e. 15 × 9 neighbouring points (with each point binned from 5 × 5 pixels). The red line corresponds to a reference power-law function fitted from experimental data at $x/d = 132$ and $R = 0W_f$.
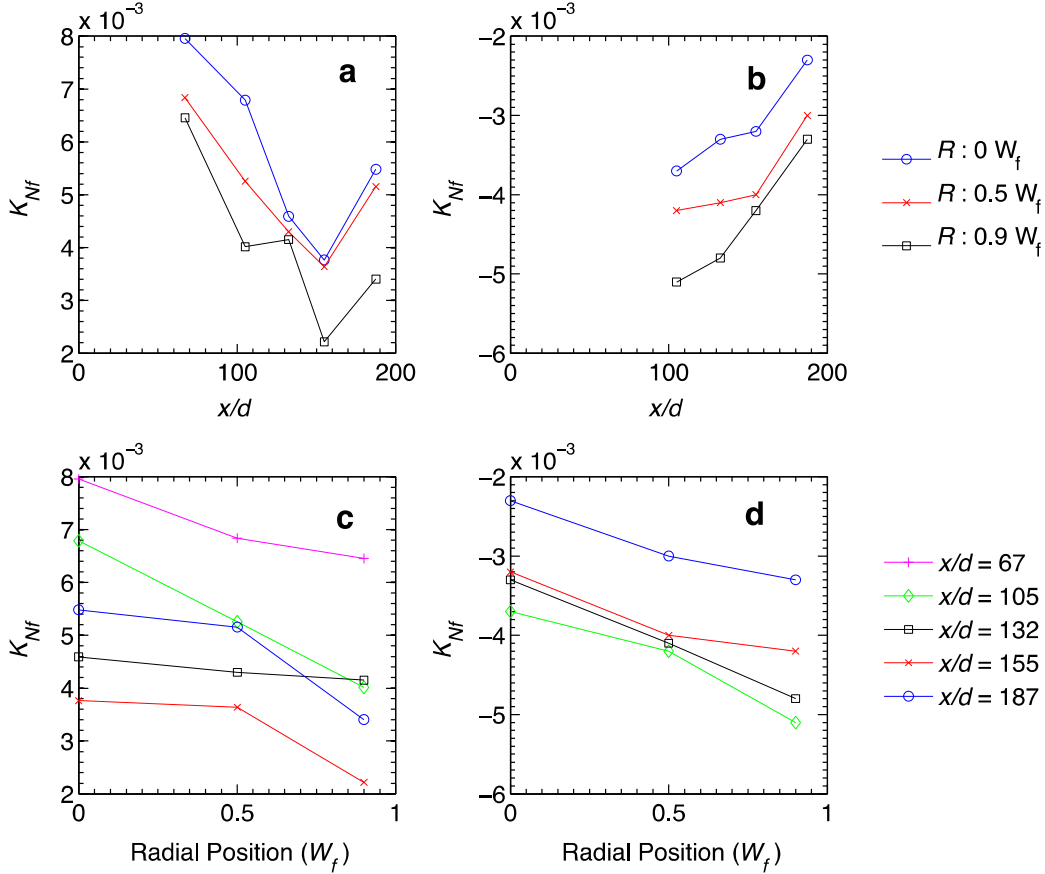

Figure 13: Coefficients of the fitted power-law function for experimental data between N_p and f_v, along (a and b) the axial and (c and d) radial direction. The coefficients are for $f_v < 0.4$ ppm (a and c) and $f_v > 0.4$ ppm (b and d).

Figure 14 presents the joint PDFs between N_p and d_p. A strong correlation can be seen between N_p and d_p at all selected locations. At the base of the flame ($x/d = 67$ and 105), N_p increases with the increase of d_p for $d_p < 12$ nm, indicating that the soot inception by coagulation of PAHs is taking place in these regions. At downstream and outer radial locations, where $d_p > 12$ nm, N_p decreases with the increase of d_p. This is consistent with an increased significance in coagulation and growth. This finding is also consistent with previous findings in the laminar flame that zones with high N_p contain particles with small d_p [14, 48, 49]. It is worth noting that at $x/d = 132$ and 155, the most probable value of N_p decreases from 5.0×10^{17} m^{-3} to 1.0×10^{17} m^{-3} from the central flame region towards the flame edge, while the corresponding most probable d_p is shifted from 30 nm to 50 nm, indicating that the large soot particles are brought by turbulent transport rather than formed by coagulation of small soot particles, consistent with previous findings [14]. The correlation between N_p and d_p can be described by a power-law function: $N_p(d_p) = a \times d_p{}^b$. A reference power-law function, which is calculated from the PDF at $x/d = 132$ and $R = 0.5W_f$, was plotted against experimental data in all subfigures in Fig. 14, to identify the trend of the PDFs for

$d_p > 12$ nm. Figure 15 presents the coefficient, b, here denoted K_{Nd}, for selected axial and radial locations. It can be found that the value of K_{Nd} increases with flame heights at all three selected radial locations, i.e. the decrease in N_p with the increase of d_p decreases at downstream locations when compared to upstream locations, as shown in Fig. 15a. The decrease in N_p with an increase in d_p decreases from the centreline of the flame towards the flame edge at $x/d = 105$ and $x/d = 132$, as shown in Fig. 15b. At the flame tip, the decrease in N_p with an increase of d_p is almost same for all selected radial locations.
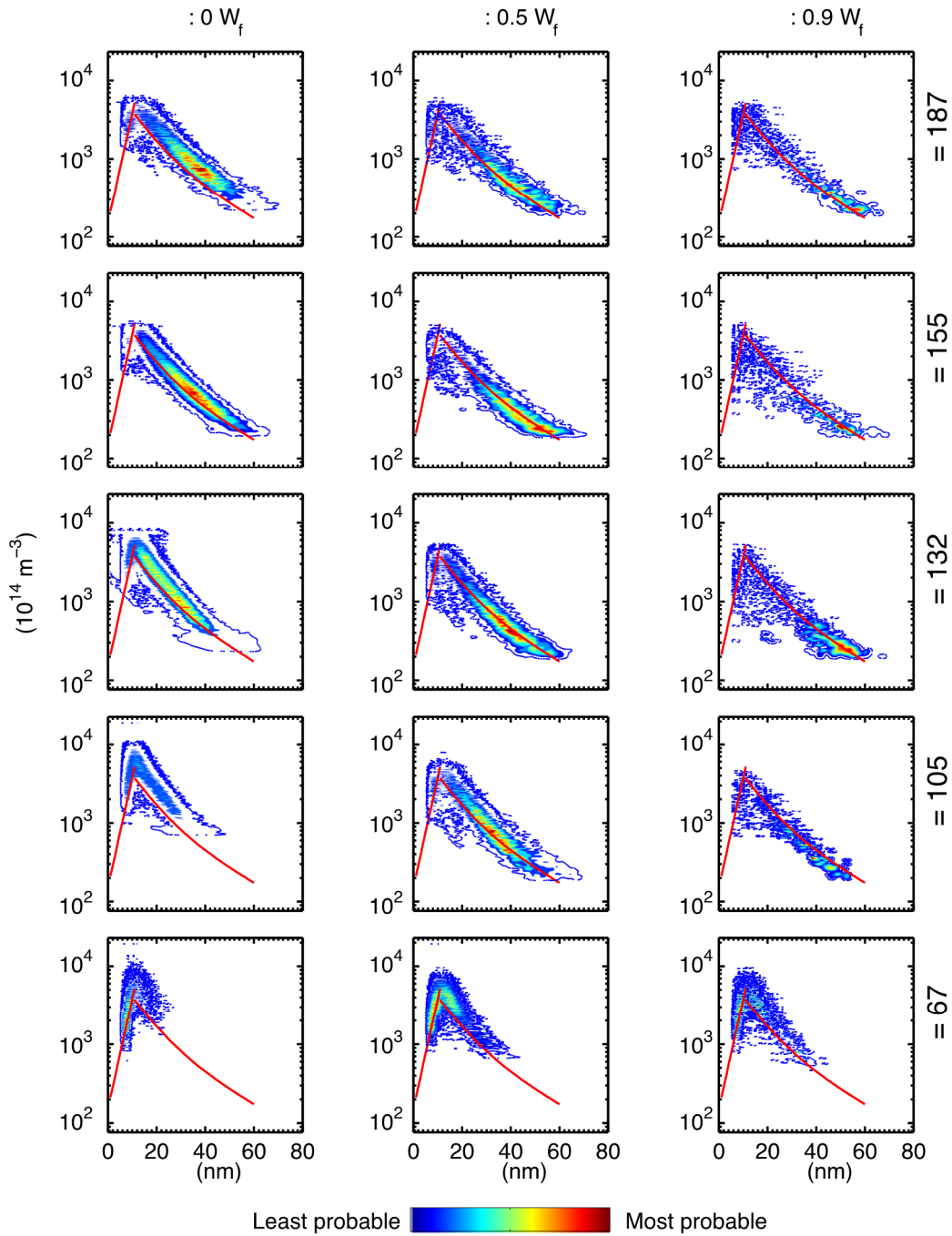

Figure 14: Joint PDFs of N_p and d_p at selected axial and radial locations. Statistics were calculated from 499 image-sets over an area of

5 (radial) $\times$ 3 (axial) mm^2, i.e. 15 $\times$ 9 neighbouring points (with each point binned from 5 $\times$ 5 pixels). The red line corresponds to a reference power-law function fitted from experimental data at $x/d = 132$ and $R = 0.5W_f$.
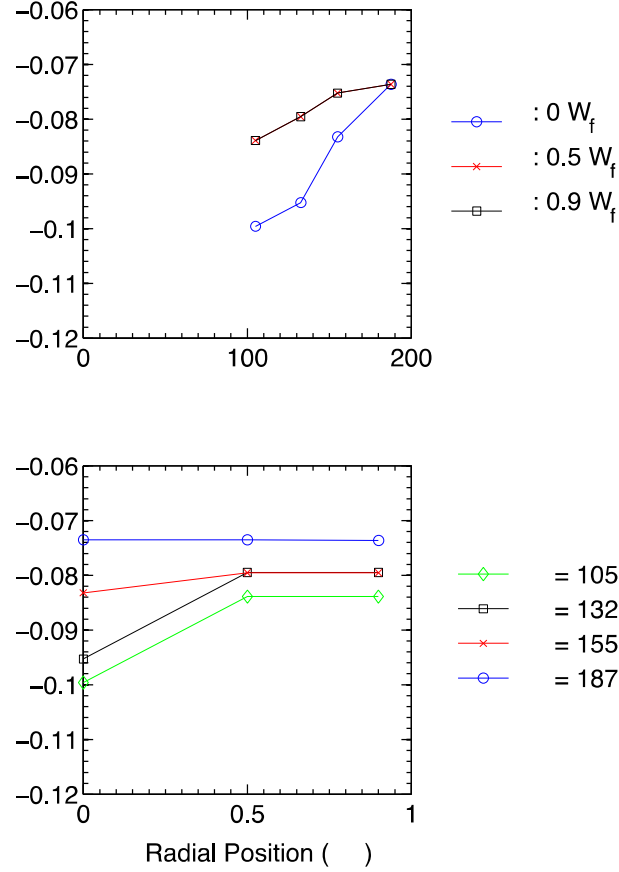

Figure 15: Coefficients of the fitted exponential function for experimental data between N and d_p, along (a) the axial and (b) radial direction.

4. Conclusions

The current simultaneous measurements of T, f_v, d_p and N_p with the nTLAF and TiRe-LII techniques yield generally very good agreement with previous measurements of T and f_v in a well-characterised turbulent ethylene sooting flame obtained using CARS and PLII [17] and also provide significant new insight. The most probable temperature matches previous measurements to within 30 K, while the mean temperatures agree well at those locations where the more than 90% of the data are within the detection limit. A criterion has also been determined that enables unambiguous determination of where unconditional statistics obtained with nTLAF are reliable, i.e. where the upper-bound and lower-bound calculations of the mean temperature converge. For the present flame, this condition applies for most of the central region of the flame. The PDF of the temperature measurements also agree well for the nTLAF and CARS measurements where the spatial resolution is similar. However, the desirability of a further increase in both the spatial resolution and signal-to-noise ratio was highlighted, with the measurements being sensitive to these parameters.

The present measurements have provided the mean and RMS values of T, f_v, d_p and N_p along the flame centreline and radial profiles at various flame heights, which can be used for the

validation of the mechanisms of soot formation and oxidation in turbulent flames. Moreover, the key findings from the joint PDFs of T, f_v, d_p and N_p in the present work are as follows:

1. The joint PDF of T and f_v reveals a significant dependence on radial distance near to the base of the flame, beyond which the dependence is mainly on axial distance. This finding is broadly consistent with previous findings [18].

2. Both the qualitative trends and quantitative values of the joint PDF of T and f_v appear to be consistent with previous independent optical measurements [10], given the differences in the flames and measurement techniques. It was found soot is typically formed between 1400 and 2000 K with the peak f_v occurring between 1550 and 1750 K on the axis.

3. From the joint PDFs of T and f_v, the value of T corresponding to the most probable f_v increases along the axis from one fourth to three quarter of the flame, while the most probable f_v at these locations was found to be $\sim 0.05 \pm 0.04$ ppm and three to five times lower than the mean f_v values. The distribution of temperature is widest at the most probable value of f_v values at all selected flame locations and is widest at the middle of the flame where f_v peaks.

4. A strong correlation was found between d_p and f_v for all selected flame locations and this relationship can be well described by a power-law function that varies little throughout the flame. Nevertheless, the range of d_p increases significantly with both radial and axial distance, particularly the latter. The most probable d_p is between 8 and 18 nm and the corresponding most probable f_v is between 0.1 and 0.5 ppm. Soot particles with $d_p > 30$ nm mostly corresponds to $f_v > 1$ ppm.

5. The joint PDFs between T and d_p reveals that the small soot particles distribute in a wider temperature range than the larger soot particles. The large soot particles are found at relatively low temperatures.

6. A moderate correlation was found between N_p and T, which varies with both radial and axial distance through the flame. The most probable N_p is between 10^{16} and 10^{17} m^{-3}, and decreases from the flame axis towards the flame edge, while the corresponding most probable T varies with flame locations.

7. A strong correlation was found between:

   a. The relationship between N_p and f_v varies little throughout the flame for all selected flame locations. The joint PDFs of N_p and f_v show that N_p increases with an increase in f_v for $f_v < 0.4$ ppm and then decreases when f_v exceeds 0.4 ppm, with a maximum value of $N_p \sim 5.0 \times 10^{17}$ m^{-3};

   b. The relationship between N_p and d_p varies little throughout the flame for all selected flame locations. It was also found that N_p increases with an increase in d_p for $d_p < 12$ nm and decreases for $d_p > 12$ nm.

5. Acknowledgments

acknowledge Dr. Geigle and Dr. Köhler from the DLR, for their willing cooperation in providing detailed information of the geometry of their burner.

6. References

[1] T.C. Bond, S.J. Doherty, D. Fahey, P. Forster, T. Berntsen, B. DeAngelo, M. Flanner, S. Ghan, B. Kärcher, D. Koch, Bounding the role of black carbon in the climate system: A scientific assessment, J. Geophys. Res. 118 (2013) 5380-5552.

[2] C. de Haar, I. Hassing, M. Bol, R. Bleumink, R. Pieters, Ultrafine carbon black particles cause early airway inflammation and have adjuvant activity in a mouse allergic airway disease model, Toxicol. Sci 87 (2005) 409-418.

[3] M.R. Heal, P. Kumar, R.M. Harrison, Particles, air quality, policy and health, Chem. Soc. Rev. 41 (2012) 6606-6630.

[4] R.L. Vander Wal, LIF-LII measurements in a turbulent gas-jet flame, Experiments in fluids 23 (1997) 281-287.

[5] S.-Y. Lee, S.R. Turns, R.J. Santoro, Measurements of soot, OH, and PAH concentrations in turbulent ethylene/air jet flames, Combust. Flame 156 (2009) 2264-2275.

[6] V. Narayanaswamy, N. Clemens, Simultaneous LII and PIV measurements in the soot formation region of turbulent non-premixed jet flames, Proc. Combust. Inst. 34 (2013) 1455-1463.

[7] A. Coppalle, D. Joyeux, Temperature and soot volume fraction in turbulent diffusion flames: measurements of mean and fluctuating values, Combust. Flame 96 (1994) 275-285.

[8] C.R. Shaddix, J. Zhang, W. Scheffer, J. Doom, J.C. Oefelein, S. Kook, L.M. Pickett, H. Wang, Understanding and predicting soot generation in turbulent non-premixed jet flames, Sand2010-7178, Sandia Report, (2010).

[9] Y. Sivathanu, G.M. Faeth, Temperature/soot volume fraction correlations in the fuel-rich region of buoyant turbulent diffusion flames, Combust. Flame 81 (1990) 150-165.

[10] C.R. Shaddix, J. Zhang. Joint temperature-volume fraction statistics of soot in turbulent non-premixed jet flames, Proceedings of the 8th US Combustion Meeting (2013).

[11] L. Gritzo, Y. Sivathanu, W. Gill, Transient Measurements of Radiative Properties, Soot volume fraction and soot temperature in a large pool fire, Combust. Sci. Technol. 139 (1998) 113-136.

[12] J.J. Murphy, C.R. Shaddix, Soot property measurements in a two-meter diameter JP-8 pool fire, Combust. Sci. Technol. 178 (2006) 865-894.

[13] H. Bockhorn, H. Geitlinger, B. Jungfleisch, T. Lehre, A. Schön, T. Streibel, R. Suntz, Progress in characterization of soot formation by optical methods, Phys. Chem. Chem. Phys. 4 (2002) 3780-3793.

[14] H. Geitlinger, T. Streibel, R. Suntz, H. Bockhorn, Two-dimensional imaging of soot volume fractions, particle number densities, and particle radii in laminar and turbulent diffusion flames, Symp. (Int.) Combust. 27 (1998) 1613-1621.

[15] B. Yang, U.O. Koylu, Detailed soot field in a turbulent non-premixed ethylene/air flame from laser scattering and extinction experiments, Combust. Flame 141 (2005) 55-65.

[16] G. Nathan, P.A.M. Kalt, Z.T. Alwahabi, B.B. Dally, P.R. Medwell, Q.N. Chan, Recent advances in the measurement of strongly radiating, turbulent reacting flows, Prog. Energy Combust. Sci. 38 (2012) 41-61.

[17] M. Köhler, K. Geigle, W. Meier, B. Crosland, K. Thomson, G. Smallwood, Sooting turbulent jet flame: characterization and quantitative soot measurements, Appl. Phys. B 104 (2011) 409-425.

[18] S.M. Mahmoud, G.J. Nathan, P.R. Medwell, B.B. Dally, Z.T. Alwahabi, Simultaneous planar measurements of temperature and soot volume fraction in a turbulent non-premixed jet flame, Proc. Combust. Inst. 35 (2015) 1931-1938.

[19] N. Qamar, Z. Alwahabi, Q. Chan, G. Nathan, D. Roekaerts, K. King, Soot volume fraction in a piloted turbulent jet non-premixed flame of natural gas, Combust. Flame 156 (2009) 1339-1347.

[20] J. Zhang, C.R. Shaddix, R.W. Schefer, Design of "model-friendly" turbulent non-premixed jet burners for C2+ hydrocarbon fuels, Rev. Sci. Instrum 82 (2011) 074101.

[21] M. Köhler, K.-P. Geigle, T. Blacha, P. Gerlinger, W. Meier, Experimental characterization and numerical simulation of a sooting lifted turbulent jet diffusion flame, Combust. Flame 159 (2012) 2620-2635.

[22] R.S. Barlow, Laser diagnostics and their interplay with computations to understand turbulent combustion, Proc. Combust. Inst. 31 (2007) 49-75.

[23] M. Di Domenico, P. Gerlinger, M. Aigner, Development and validation of a new soot formation model for gas turbine combustor simulations, Combust. Flame 157 (2010) 246-258.

[24] Q.N. Chan, P.R. Medwell, P.A. Kalt, Z.T. Alwahabi, B.B. Dally, G.J. Nathan, Simultaneous imaging of temperature and soot volume fraction, Proc. Combust. Inst. 33 (2011) 791-798.

[25] B. Axelsson, R. Collin, P.-E. Bengtsson, Laser-induced incandescence for soot particle size and volume fraction measurements using on-line extinction calibration, Appl. Phys. B 72 (2001) 367-372.

[26] R. Hadef, K.P. Geigle, J. Zerbs, R.A. Sawchuk, D.R. Snelling, The concept of 2D gated imaging for particle sizing in a laminar diffusion flame, Appl. Phys. B 112 (2013) 395-408.

[27] B. Hu, B. Yang, U.O. Koylu, Soot measurements at the axis of an ethylene/air non-premixed turbulent jet flame, Combust. Flame 134 (2003) 93-106.

[28] Ü.Ö. Köylü, C.S. McEnally, D.E. Rosner, L.D. Pfefferle, Simultaneous measurements of soot volume fraction and particle size/microstructure in flames using a thermophoretic sampling technique, Combust. Flame 110 (1997) 494-507.

[29] H. Oltmann, J. Reimann, S. Will, Single-shot measurement of soot aggregate sizes by wide-angle light scattering (WALS), Appl. Phys. B 106 (2012) 171-183.

[30] E. Cenker, K. Kondo, G. Bruneaux, T. Dreier, T. Aizawa, C. Schulz, Assessment of soot particle-size imaging with LII at Diesel engine conditions, Appl. Phys. B 119 (2015) 765-776.

[31] Z. Sun, D. Gu, G. Nathan, Z. Alwahabi, B. Dally, Single-shot, Time-Resolved planar Laser-Induced Incandescence (TiRe-LII) for soot primary particle sizing in flames, Proc. Combust. Inst. 35 (2015) 3673-3680.

[32] P.R. Medwell, Q.N. Chan, P.A. Kalt, Z.T. Alwahabi, B.B. Dally, G.J. Nathan, Development of temperature imaging using two-line atomic fluorescence, Appl. Opt 48 (2009) 1237-1248.

[33] Q.N. Chan, P.R. Medwell, B.B. Dally, Z.T. Alwahabi, G.J. Nathan, New seeding methodology for gas concentration measurements, Appl. Spectrosc. 66 (2012) 803-809.

[34] D.H. Gu, Z.W. Sun, P.R. Medwell, Z.T. Alwahabi, B.B. Dally, G.J. Nathan, Mechanism for laser-induced fluorescence signal generation in a nanoparticle-seeded flow for planar flame thermometry, Appl. Phys. B 2 (2015) 209-218.

[35] D. Gu, Z. Sun, G.J. Nathan, P.R. Medwell, Z.T. Alwahabi, B.B. Dally, Improvement of precision and accuracy of temperature imaging in sooting flames using two-line atomic fluorescence (TLAF), Combust. Flame 167 (2015) 481-493.

[36] C. Schulz, B.F. Kock, M. Hofmann, H. Michelsen, S. Will, B. Bougie, R. Suntz, G. Smallwood, Laser-induced incandescence: recent trends and current questions, Appl. Phys. B 83 (2006) 333-354.

[37] H. Bladh, J. Johnsson, P.-E. Bengtsson, On the dependence of the laser-induced incandescence (LII) signal on soot volume fraction for variations in particle size, Appl. Phys. B 90 (2008) 109-125.

[38] A. D'Anna, A. Rolando, C. Allouis, P. Minutolo, A. D'Alessio, Nano-organic carbon and soot particle measurements in a laminar ethylene diffusion flame, Proc. Combust. Inst. 30 (2005) 1449-1456.

[39] K. Tian, F. Liu, K.A. Thomson, D.R. Snelling, G.J. Smallwood, D. Wang, Distribution of the number of primary particles of soot aggregates in a nonpremixed laminar flame, Combust. Flame 138 (2004) 195-198.

[40] S. Schraml, S. Dankers, K. Bader, S. Will, A. Leipertz, Soot temperature measurements and implications for time-resolved laser-induced incandescence (TIRE-LII), Combust. Flame 120 (2000) 439-450.

[41] J.E. Sansonetti, W. Martin, Handbook of basic atomic spectroscopic data, J. Phys. Chem. Ref. Data 34 (2005) 1559-2259.

[42] J. Engström, J. Nygren, M. Aldén, C. Kaminski, Two-line atomic fluorescence as a temperature probe for highly sooting flames, Optics Letters 25 (2000) 1469-1471.

[43] Z. Sun, Z. Alwahabi, D. Gu, S. Mahmoud, G. Nathan, B. Dally, Planar laser-induced incandescence of turbulent sooting flames: the influence of beam steering and signal trapping, Appl. Phys. B 119 (2015) 731-743.

[44] J. Zerbs, K. Geigle, O. Lammel, J. Hader, R. Stirn, R. Hadef, W. Meier, The influence of wavelength in extinction measurements and beam steering in laser-induced incandescence measurements in sooting flames, Appl. Phys. B 96 (2009) 683-694.

[45] C.J. Dasch, D.M. Heffelfinger, Planar imaging of soot formation in turbulent ethylene diffusion flames: fluctuations and integral scales, Combust. Flame 85 (1991) 389-402.

[46] K. Netzell, H. Lehtiniemi, F. Mauss, Calculating the soot particle size distribution function in turbulent diffusion flames using a sectional method, Proc. Combust. Inst. 31 (2007) 667-674.

[47] B. Zhao, Z. Yang, Z. Li, M.V. Johnston, H. Wang, Particle size distribution function of incipient soot in laminar premixed ethylene flames: effect of flame temperature, Proc. Combust. Inst. 30 (2005) 1441-1448.

[48] A. Gomez, M. Littman, I. Glassman, Comparative study of soot formation on the centerline of axisymmetric laminar diffusion flames: fuel and temperature effects, Combust. Flame 70 (1987) 225-241.

[49] B. Zhao, Z. Yang, M.V. Johnston, H. Wang, A.S. Wexler, M. Balthasar, M. Kraft, Measurement and numerical simulation of soot particle size distribution functions in a laminar premixed ethylene-oxygen-argon flame, Combust. Flame 133 (2003) 173-188.